

**Generation and characterization of functionalized
organic nanoaggregates.**

Ph.D. Thesis
MCI-Mads Clausen Institute
University of Southern Denmark

Christian Maibohm

July 26, 2010

Chapter 1

Preface

This thesis represent the final part of the requirements for achieving the Ph.D. degree at the University of Southern Denmark and was carried out in the period 2007 to 2010. The first two years of this work was carried out at the Mads Clausen Institute at SDU in Sønderborg and the last year was carried out at Carl-Von-Ossietzky university in Oldenburg, Germany. At the Mads Clausen institute I have been part of the NanoSYD group working under the supervision of Professor Horst-Günter Rubahn. In Oldenburg I have been part of the AL-Shamery working group under the supervision of Professor Katharina Al-Shamery. Apart from this thesis, publications and other presentation works have also been made during this project, these are listed in appendix A.

I would like to thank and acknowledge several people and groups for their support and collaboration during my Ph.D. project. First and foremost my supervisor Professor Horst-Günter Rubahn for his constant support and assistance on many aspects during the project. Professor Katharina Al-Shamery for her support and giving me the possibility to and conduct experiments in her lab in Oldenburg. Maren Rastedt for good collaboration and her constant supply of template assisted nanostructures for my characterization experiments. My colleagues at NanoSYD for their support and discussions about ideas and scientific problems during the project. My colleagues at the Al-Shamery working group in Oldenburg for their help, support and good collaboration. Also a big thanks to them for making a foreigner very welcome in their group. Jonathan Brewer from MEMPHYS for technical support and good ideas.

During my project I have also been working together with the S. Tamulevicius group from the Institute of Physical Electronics, Kaunas University of Technology, Lithuania to whom I owe thanks.

Last but not least my family who have been a constant support during the whole project.

Chapter 2

Abstract

One dimensional semiconducting nanostructures have attracted increasing interest for the last decade due to their prospect of increasing performance, adding special properties and lowering material consumption when incorporated into devices[1, 2, 3, 4, 5]. In this work, two different 1D nanostructures have been studied with a main focus on their optical properties.

One nanostructure consists of organic molecular beam epitaxy(OMBE) grown, single-crystallin para-hexaphenylene nanofibers which are oriented parallel to the surface plane. The nanofibers have been shown to behave as optical waveguides[6, 7, 8, 9] while other properties like frequency doubling[10] and lasing[11] have also been observed in these structures. The other nanostructure consists of template assisted grown nanostructures from the small organic molecule Tbf(17H-Tetrabenzo[a,c,g,i]fluoren). These nanostructures are oriented perpendicularly to the surface plane and they have a tube-like geometry. Hence they are meant to act as the outer shell of core shell structures. Using a two-step fabrication process the first core shell structures have been fabricated with an outer shell of Tbf and a core consisting of another small organic molecule.

Optical investigations of the template assisted nanostructures have shown that they can act as optical waveguides like para-hexaphenylene nanofibers.

An important part of the project was to design and build a femtosecond laser scanning microscope(LSM). Due to its ability to make spatially very well (below 250 nm) localized excitation with very high peak energy the LSM is expected to be an important optical characterization tool, especially when combined with a near field optical scanning microscope (SNOM). Both LSM and SNOM have been applied to functionalized nanofibers.

Characterization of the core shell structures shows changed optical properties as compared to the unfilled structures, which demonstrates that core shell structures represent a way to specifically tailor 1D nanostructures to specific purposes. In addition to providing detailed information about the specific nanostructures in the project, the obtained results also demonstrate

the usefulness of laser scanning microscopy as a technique for optical characterization of nanostructures.

Chapter 3

Dansk resumé

En-dimensionale halvleder nanostrukturer har i de seneste år tiltrukket stor bevågenhed grundet deres store potential for øgede ydeevne, specielle egenskaber og en sænkning af materiale omkostningerne når de indbygges i opstillinger. I dette arbejde er to forskellige 1D nanostrukturer blevet undersøgt, hvor fokus hovedsageligt har været på de optiske egenskaber. Den ene nanostruktur består af Organic Molecular Beam Epitaxy(OMBE) fremstillede, enkelt krystalinske para-hexaphenylene nanofibre. Disse nanofibre har vist at have bølgeledende egenskaber, at kunne virke som frekvensdobler og som lasing materiale. Den anden af de undersøgte strukturer er templat fremstillede nanorør af et lille organisk molekyle kaldet Tbf(17H-Tetrabenzo[a,c,g,i]fluoren). Disse nanorør er fremstillet så de kan virke som det yderste lag i en så kaldt core shell struktur. Disse core shell strukturer fremstilles i en to-trins proces hvor Tbf bliver brugt som den ydre skal og kernen i strukturen vil være et andet organisk molekyle. De optiske undersøgelser af disse nanorør har vist at de kan fungere som bølgeledere ligesom nanofibrene af para-hexaphenylene. En stor del af projektet har været at designe og bygge et laser scanning mikroskop(LSM). Med dette mikroskop er man i stand til både, at eksitere prøver i det optiske lineære regime og grundet den høje spids energi også i det optiske ikke-lineære regime. I dette projekt har mikroskopet indgået i de optiske undersøgelser sammen med andre instrumenter, så som et scanning nær-feldt mikroskop(SNOM). De optiske undersøgelser foretaget i dette projekt demonstrerer at core shell strukturer er en måde hvorpå nanostrukturer kan få skræddersyet egenskaber for at opfylde en specifik opgave. Projektet viser også, at LSM'et er et vigtigt instrument til undersøgelse og forståelse af de optiske egenskaber af nanostrukturer.

Contents

1	Preface	3
2	Abstract	5
3	Dansk resumé	7
4	Introduction	11
4.1	Nanotechnology	11
4.2	1D nanostructures	11
5	Experimental instrumentation	13
5.1	Laser scanning microscope	13
5.2	Scanning of nanostructures	20
5.3	Low temperature spectroscopy	21
5.4	EPI-fluorescence microscope	23
5.5	SEM	24
6	Organic 1D nanostructures	25
6.1	Surface grown para-phenylene nanoaggregates	25
6.1.1	Introduction	25
6.1.2	The molecular unit	26
6.1.3	Para-hexaphenylene in the solid phase	26
6.1.4	p-6P on mica	27
6.1.5	Fabrication of para-phenylene nanoaggregates on mica	29
6.2	Template assisted grown nanostructures	30
6.2.1	Introduction	30
6.2.2	The molecular units and crystals	30
6.2.3	Templates	31
6.2.4	Fabrication method	32
6.2.5	Template removal	34
6.3	Summary	35

7	Linear optical characterization	39
7.1	Introduction	39
7.2	Room temperature observations	39
7.3	Low temperature spectroscopy	43
7.3.1	Introduction	43
7.4	Spectra of para-hexaphenylene	43
7.4.1	Para-hexaphenylene in powder form	43
7.4.2	Para-hexaphenylene nanoaggregates	46
7.5	Spectra of Tbf and Tms-tbf	46
7.5.1	Starting materials	46
7.5.2	Spectra of nanoaggregates	48
7.5.3	Core shell structures	51
7.6	Thermal decomposition	51
7.7	Summary	57
8	Waveguiding in 1D nanostructures	59
8.1	Introduction	59
8.2	Experimental setup for waveguiding	61
8.3	Waveguiding in p-6P nanofibers	63
8.4	Waveguiding in PPTPP nanofibers	64
8.5	Waveguiding in nanotubes	67
8.5.1	Waveguiding in Tbf nanotubes	67
8.6	Waveguiding in Tms-tbf nanotubes	69
8.7	Summary	71
9	Conclusions and outlook	73
9.1	LSM	73
9.2	Low temperature spectroscopy	73
9.3	Waveguiding	73
9.4	Outlook	74
A	Publication list	75
A.1	Publication list	75
A.1.1	Refereed	75
A.1.2	Refereed conference proceeding	75
A.1.3	Articles to be submitted	75
A.2	Posters	76
A.3	Presentations	76

Chapter 4

Introduction

4.1 Nanotechnology

Since the middle of last century electronic industry has driven the development of electronic components towards smaller and smaller sizes, sometimes referred to as 'Moore's law'[12]. This microminiaturization has been performed mainly via lithographic techniques and thus represents a generic top down approach ('from large to small'). This method is limited mainly by technological problems, which in fact can be solved by clever engineering down to an impressively small size. Intel already now routinely breaks the 30 nm size limit. This rapid nano-miniaturization results in an integration of more than a few ten million logic elements on a single chip.

However, approaching atom dimensions, new limits are set by physical laws which gain increasing importance with decreasing size. Also, the complexity of the systems to be mastered on a nano-level increases tremendously. Hence another approach has become important, the 'bottom-up' approach ('from small to large'). Here, nano-sized objects are formed from their atomic or molecular compounds using appropriate building recipes. A huge advantage of the 'bottom-up' approach as compared to the 'top-down' approach is that it is a massive parallel approach. Every product mol unit contains some 10^{23} individual but identically built nano systems. With the 'bottom-up' approach and novel materials nanostructures with well-defined size, shape and unique properties can be fabricated.

4.2 1D nanostructures

One dimensional (1-D) nanostructures are objects with a height and width below 100 nm, whereas the aspect ratio is large. The literature holds many examples of 1-D nanostructures in the form of nanotubes, nanoribbons, nanowires, nanofibers and many more. In the recent years, such 1-D nanostructures have obtained a huge interest within the scientific community,

due to their large application potential within for instance sensing, optoelectronics and photonics[1, 2, 4, 5, 3]. In this thesis two 1D nanostructures have been investigated to characterize their optical properties.

Chapter 5

Experimental instrumentation

5.1 Laser scanning microscope

Part of this Ph.D project has been to design and build a two photon laser scanning microscope (LSM) at the Mads Clausen institute in Sønderborg. The idea was to take a standard inverted fluorescence microscope and build a versatile instrument in which both single and multi photon processes could be investigated.

The microscope unit

The main building block chosen for the LSM was an inverted Nikon Eclipse TE 2000U microscope which came equipped with infinity corrected objectives (4X, 10X, 20X and 40X) and a filter block containing an excitation filter for 340-380 nm and a dichroic mirror for 400 nm. The microscope was equipped with a high pressure mercury lamp as excitation source and with the mentioned excitation filter the single photon excitation is centered at 365 nm.

In order to accommodate optics for the laser scanning part and thereby incoupling of the Ti:sapphire femtosecond laser source (Spectra Physics Tsunami, broadband 710-980nm) an additional layer was added to the inverted microscope. The two optical components mounted in the filter block for the two photon excitation are: 1) a laser beam splitter (T: 310-680 nm > 90% and R: 720-1050 nm > 90%) which directs the laser beam to the objective and let collected light from the sample pass. 2) an emitter filter (T: 350-650 nm > 90% and blocking > OD8 for 680-1040 nm) which effectively blocks the excitation light. The two layer configuration together with the optical components inside the microscope are seen in figure 5.1. The two layer configuration makes the switching between single and two photon excitation

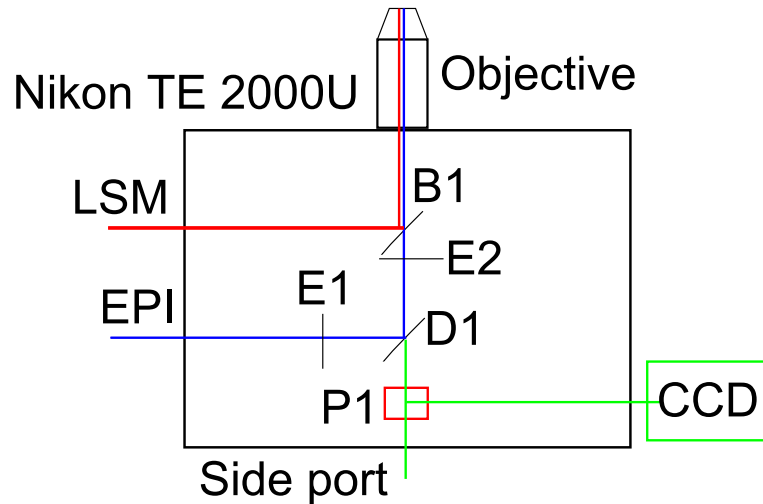


Figure 5.1: Schematic drawing of the two excitation paths (blue: single photon and red: two photon) and the detection path (green) inside the inverted microscope. The optical components are: E1: excitation filter(340-380 nm), D1: dichroic mirror(400 nm), B1: laser beam splitter(T: 310-680 nm > 90% and R: 720-1050 nm > 90%), E2: emitter filter(T: 350-650 nm > 90% and blocking > OD8 for 680-1040 nm) and P1 is the port selecting prism.

effortless with no need to align additional optical components and also offers the possibility of illuminating the sample with both excitation sources at the same time.

Scanning optics and principle

The basic principle behind laser scanning microscopy is to raster a diffraction limited laser spot over the sample and simultaneously collect light from the exact same spot. The collected light from each point is then sent to a detector and combined by software to form an image of the scanned area on a computer. The scanning part of the microscope was constructed on ideas from a microscopes built by Jonathan Brewer[13] and along lines described in[14].

To design a optical train of components which makes and raster a diffraction limited spot in the object plane I will look at the optical components in reverse order and start with the spot or point. A point in the object plane will be converted into a parallel beam by the infinity corrected objectives so there is no intermediate image plane created by the objective. Three points with different location in the object plane are shown in different colors in figure 5.2. Each of them creating a parallel beam going out of the back focal plane of the objective but depending on the position in the object plane at

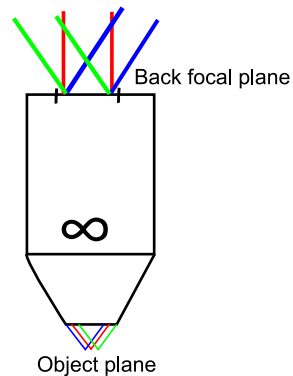


Figure 5.2: Three points in the object plane are shown in different colors. Each point creates a parallel beam out of the back focal plane of the infinity corrected objective but at a different angle. So by illuminating the back focal plane by a parallel beam and changing the angle of incidence one can raster the spot in the objective plane. The angles of incidence shown in the figure are exaggerated in order to show the principle.

a slightly different angle. Reversing this picture means that by illuminating the back focal plane of the objective by a parallel beam and changing the angle of incidence and not the position of this beam a movable spot is created in the objective plane.

A Keplerian telescope or telecentric system was constructed to produce the needed parallel beam. A Telecentric system consists of two lenses spaced at the sum of focal lengths of the individual lenses giving the telescope a magnification which depends only on the ratio of the focal lengths of the two lenses and making the magnification of the telescope space invariant. The two lenses of the telescope are a high aperture laser objective (scan lens, focal length 50 mm) and a near IR achromat lens (tube lens, focal length 200 mm) which gives the telescope a magnification of 4x. The two lenses were mounted in optical tubing with length adjustable ends so the lens separation could be set with high precision. To move or scan the created parallel beam a scan mirror is placed with its pivoting point on the optical axis of the telescope and at the focal length of the scan lens. This allows the beam to be scanned in one direction as seen left in figure 5.3, to scan both directions two scan mirrors are needed. As scanning mirrors a set of galvanometric scanners (Model 6210H scanner) fitted with 6 mm silver mirrors was used and for precise positioning the mirror unit was mounted on a x-y-z-stage. The telescope was also mounted on a x-y-z-stage so the distance from the tube lens to the back focal plane of the objective can be set to exactly the focal length of the of the tube lens (f_2), as seen on the right in figure 5.3. If the back focal plane is placed at another distance than f_2 both position and angle of incidence of the parallel beam from the telescope will be changed

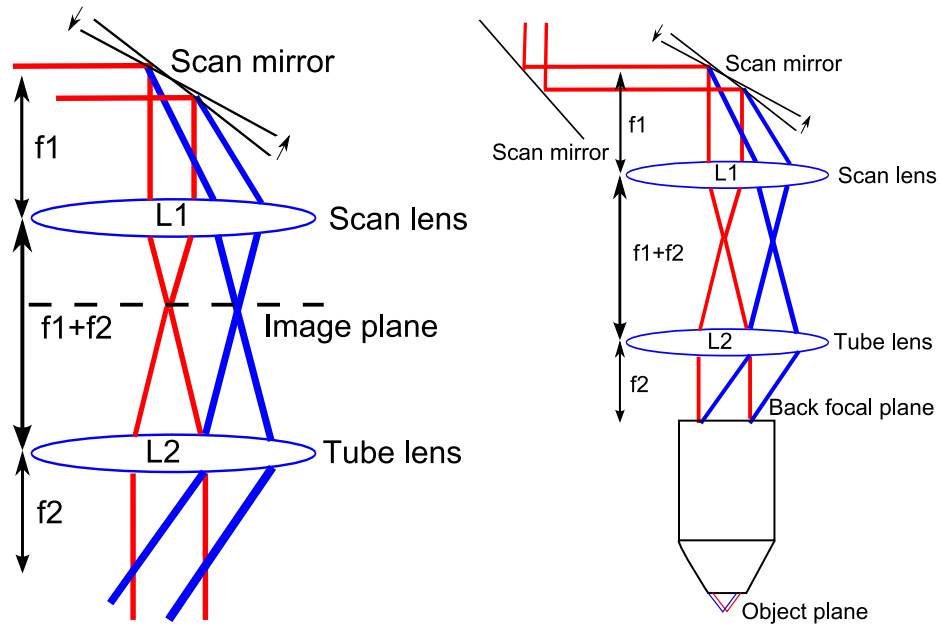


Figure 5.3: Left: Schematic drawing of the Keplerian telescope consisting of the scan lens and the tube lens placed at the sum of their focal lengths. It is seen that a tilt of the scan mirror induces a spatial movement of the beam in the image plane in the telescope. Then the light passes the tube lens which create a parallel beam and changing the spatial offset into a change of propagation angle. Right: The full optical setup for scanning a diffraction limited spot in the object plane.

as seen on the left in figure 5.3.

To get the spot to be at the diffraction limit we need to uniformly illuminate the back focal plane with a planar wave. Since the excitation laser has a Gaussian profile we need to overfill the back focal plane and for Gaussian profiles this is usually done by a factor 2, that is, the $1/e^2$ of the beam should be twice the diameter of the back focal plane[14]. The excitation laser has a $1/e^2 \approx 2$ mm but when the beam passes through the telescope it is expanded by a factor of 4 and is then larger than the back focal plane of the 40x objective which is 6.4 mm thereby fulfilling the overfilling criterion. The other objectives mounted on the microscope have back focal planes which are larger than the $1/e^2$ of the beam even after the expansion so the overfilling criterion is not fulfilled and the spot will not be diffraction limited if these objectives are used.

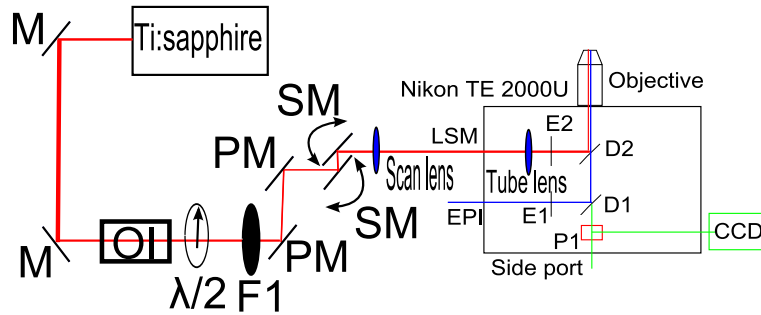


Figure 5.4: Schematic drawing of the excitation path and scanning part of the LSM. The excitation path consists of two guiding mirrors(M), an optical isolator(IO), a lambda-half plate($\lambda/2$), neutral density filter wheel(F1) and two periscope mirrors(PM).

Excitation path and scanning

The excitation path together with the scanning optics described above are shown in figure 5.4. The individual elements of the excitation path will be described in the following section. Laser light from a broadband Tsunami Ti:sapphire femtosecond laser from Spectra Physics, was used as excitation. The laser has a pulse length below 100 fs and the wavelength can be adjusted manually between 710 and 980 nm. The laser is directed towards the scanning mirrors and microscope by two adjustable guiding mirrors but before reaching the scanning mirrors the beam passes several optical elements. The first element is an optical isolator which prevents unwanted feedback from other elements back into the laser cavity which would otherwise stop the laser from pulsing. To control the intensity of the laser a neutral density filter wheel was inserted into the beam path and depending on the experiment a lambda-half plate could also be inserted to control the polarization. A periscope was needed to raise the beam to the level of the scanning mirrors and the telescope. To align the optical elements in the excitation path the laser was set to run in cw mode and pinholes was installed along the beam path for easy daily fine alignment. Scanning the spot in the object plane is done with 6210H galvanometric scanners from Cambridge Technology. Their scanning position. i.e. the mirror deflection were controlled by a A510 3-X DAC computer card from ISS. The computer card is specially made for confocal microscopy and besides controlling the scanners for x-y-directions the card also has the possibility of controlling an additional scanner for the z-direction so full 3D imaging can be performed. The investigated nanostructures in this thesis has a height up to a few hundred nanometers which is below the sectioning capability of a z-scanner for this reason the built microscope was not fitted with a z-scanner. To control the scanners the computer program "GLOBALS for imaging" developed

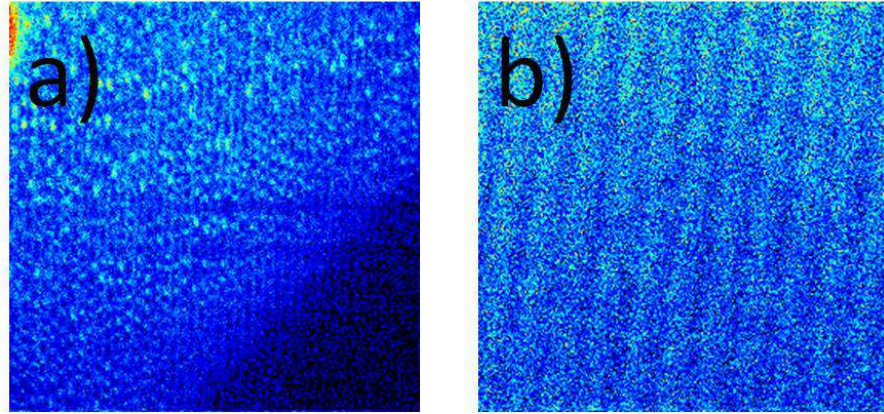


Figure 5.5: Laser scanning images of the alumina part of a recordable CD with a structure period of $1.6 \mu\text{m}$. a) scan voltage 2000 mV giving a scan area of $68.3 \times 68.3 \mu\text{m}$. The alumina foil was not perfectly flat over the whole scan area bringing the lower right corner out of focus. b) scan voltage 500 mV giving a scan area of $19.2 \times 19.2 \mu\text{m}$. The images were made with the 40x objective (NA:0.6), 64 ms scan period, 256×256 scan points and the Ti:sapphire excitation @795 nm.

by Enrico Gratton was used. The program is available from Laboratory for Fluorescence Dynamics (www.lfd.uci.edu/globals/). In the program the size of the scan area is determined by the voltage applied to the scanners. To convert the applied voltage to a size measure of the scan area a known structure was scanned at different voltages. The chosen structure was the alumina part of a standard recordable CD which has a distance between two adjacent grooves of $1.6 \mu\text{m}$ measured with by an AFM. Analysis of the structure size and period in the scanned images of the CD-sample shows a linear connection between the scanned area and the applied voltage. Two of the scanned images are shown in figure 5.5 where the applied voltage has been reduced by a factor 4 from image a) to b).

Before a scan is initiated the number of scan points and scan period is also set in the "Globals" computer program. The first is how many points the scan area is divided into, for instance 256×256 while the second is how long the excitation laser illuminate each scan point before moving to the next

Detection and imaging

Light collected from the sample passes from the back aperture of the objective through the dichroic mirror and emission filter effectively blocking the

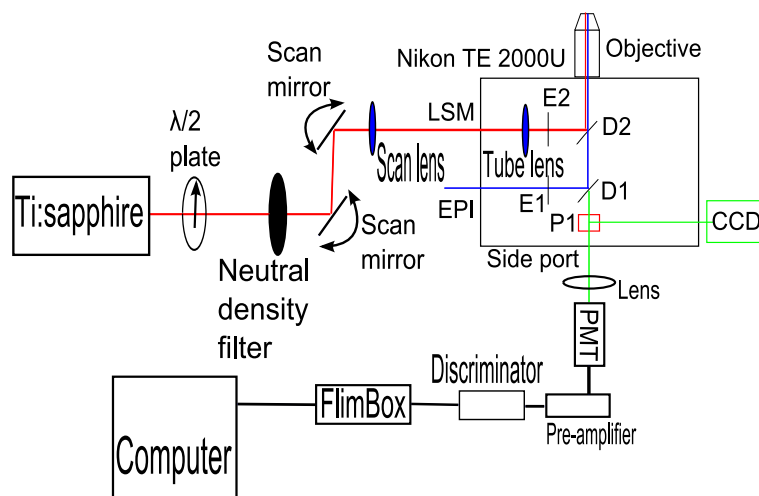


Figure 5.6: Schematic drawing of the complete LSM setup.

excitation light. After the emission filter the light can either be sent to the front port and the CCD camera or to the side port for detection with the photomultiplier tube (PMT). The complete LSM setup is seen as schematic drawing in figure 5.6 and as an image in 5.7. The CCD camera is used for several functions on the microscope but not as a detector for laser scanning, this is due to its low sensitivity and large pixel size which will give a loss of spatial resolution. The CCD is instead used for alignment of the excitation path for the LSM and in general for sample imaging when the EPI-fluorescence excitation is used. The third use of the CCD camera is to image two photon excited waveguiding in the nanostructures, which will be described in the optical characterization section of the thesis. When laser scanning the collected light from the sample is sent out of the side port and focused by a lens onto the window of a PMT. The PMT used in the setup is a Hamamatsu R585 tube which is working in the photon counting regime. The photo current from the PMT is first sent to a pre-amplifier (ESN electronic VT110 CH4) made for photon counting and then to a constant fraction timing discriminator (Phillips Scientific model 6915) which converts the signal into a TTL signal. The TTL pulses are collected by a field-programmable gate array (FPGA) which is programmed by software from the Laboratory for Fluorescence Dynamics and acts as a pulse counter [15]. The FPGA is connected to a computer where the "Globals for imaging" program mentioned above is used to combine the collected signal from each point into an image of the scanned area.

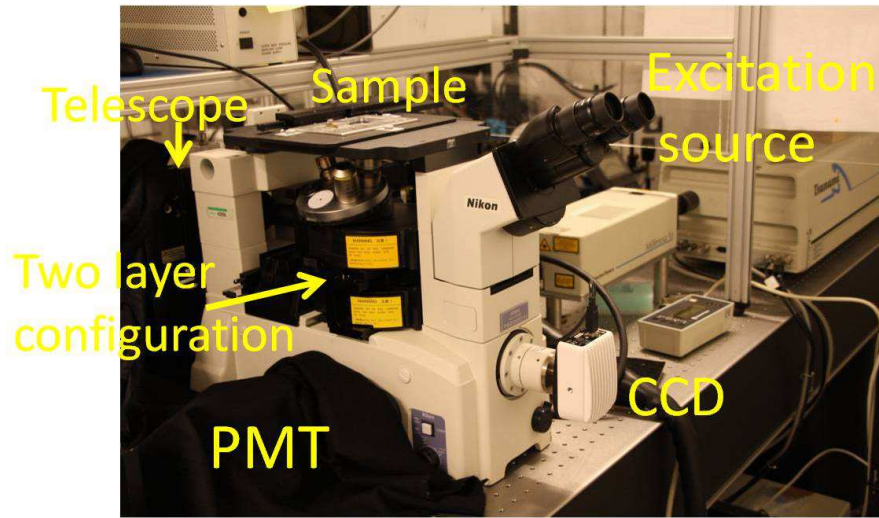


Figure 5.7: Image of the LSM setup in the lab in Sønderborg.

Resolution

To estimate the lateral resolution of the laser scanning microscope structures with known dimensions but below the spot size of the microscope are scanned and from the optical response of the system the two photon point spread function (PSF) is calculated with the "Globals for imaging" program. As scan objects fluorescent beads with a diameter of 200 nm were chosen. They were drop casted from solution on a microscope slide and an area with isolated beads was scanned. Two of the scanned images are shown in figure 5.8 and from these the calculated PSF for the system is $0.275 \mu\text{m}$ which is comparable to a similar system[13] indicating that the system is well optimized.

5.2 Scanning of nanostructures

The advantage of the LSM is its high peak energy, small focus volume and high detector sensitivity which is illustrated in the following scanning example of nanostructures. Tms-tbf nanotubes were drop casted on a microscope slide and a fluorescence image was recorded with the CCD camera, as seen in a) in figure 5.9. The low fluorescence emission combined with low sensitivity of the CCD camera limits the ability to identify individual nanostructures on the surface. If the same area is scanned with the LSM the signal to noise ratio is greatly enhanced so individual nanostructures are seen and nanostructures not seen with the standard fluorescence microscope are now detectable, as seen in b) in figure 5.9. With the LSM it is possible to reduce the scan area so details in the individual nanostructures

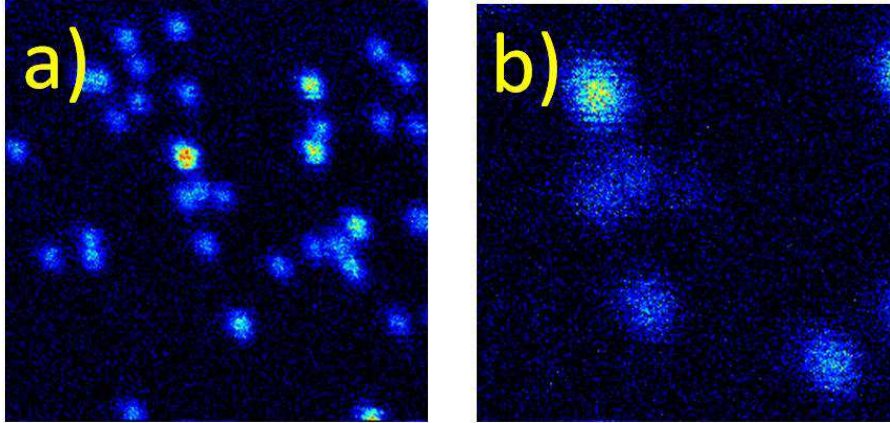


Figure 5.8: Laser scanning images of fluorescent beads with a diameter of 200 nm. From the scanned images the two photon point spread function were calculated. a) scan voltage 500 mV giving a scan area of $19.2 \times 19.2 \mu\text{m}$. b) scan voltage 200 mV giving a scan area of $8.9 \times 8.9 \mu\text{m}$. The images were made with the 40x objective(NA:0.6), 64 ms scan period, 256×256 scan points and the Ti:sapphire excitation @795 nm.

can be distinguished, as seen in c) and d) in figure 5.9. The nanostructures in the fluorescence image recorded by the CCD camera seems to be in the same focus plane which is a consequence of the excitation source and method which induces fluorescence in the full cone of the objective. This is in contrast to the LSM images where the inherent sectioning capability of the two-photon excitation process produces a very small excitation volume whereby only nanostructures in this volume are excited and detected. This makes different layers in the sample distinguishable.

5.3 Low temperature spectroscopy

The temperature dependence of the steady-state fluorescence spectra of the samples were investigated with the setup seen in figure 5.10. The samples were glued to the sample holder with silver paste for thermal conductivity and the system was evacuated to a base pressure of 10^{-5} mbar. The sample was brought down to 5 K by adiabatic cooling with liquid He and a fluorescence spectrum was made by shortly illuminating the sample with a HeCd laser. The fluorescence spectrum was recorded with a spectrometer(Acton SpectraPro-150) with a 300 g/mm grating fixed at 650 nm and a CCD camera(Princeton Pixes 100). With this setup the grating is not scanned to record a full spectra thus greatly reducing the illumination time

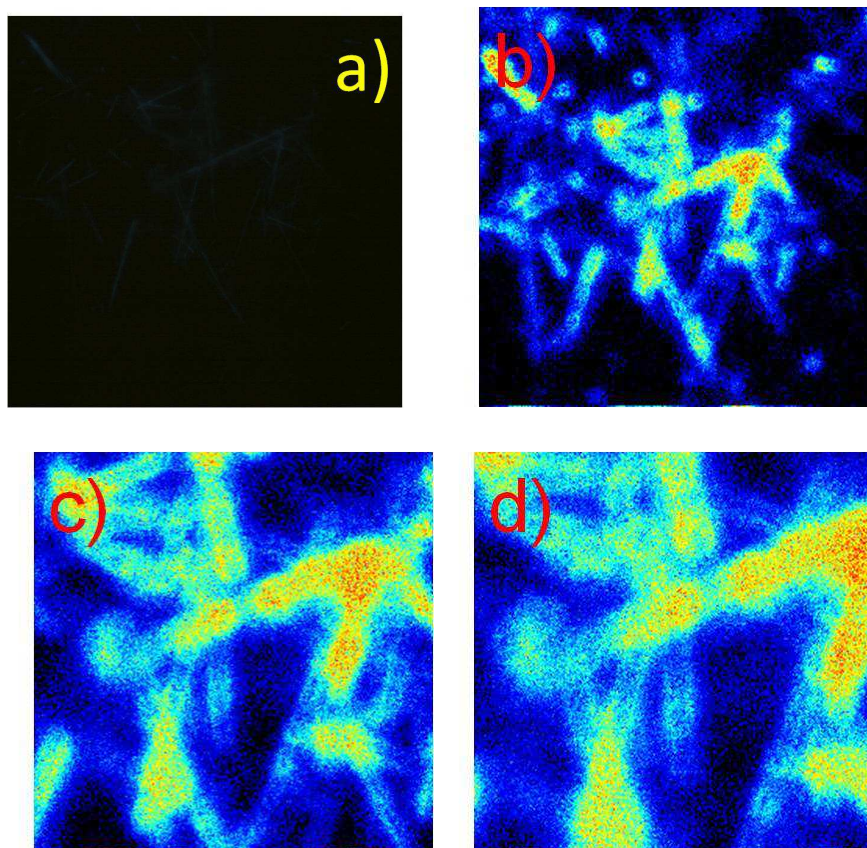


Figure 5.9: a) Fluorescence image of TMS-TBF nanotubes deposited onto a glass slide. Excitation source is a high pressure mercury lamp with emission wavelength centered at 365 nm. The sensitivity of the CCD camera and the instantaneous light intensity limits the information which can be gathered from the image. The red square is the LSM scan area shown in b). Two photon fluorescence images of the red square area in a), made with the LSM and using 800 nm femtosecond light as the excitation source. Nanotubes which are not seen in the standard fluorescence microscope become detectable with the LSM. The three images show a gradual smaller scanning area where more and more details become visible. b) Scan area $134.3 \times 134.3 \mu\text{m}$ c) Scan area $68.3 \times 68.3 \mu\text{m}$ d) Scan area $41.9 \times 41.9 \mu\text{m}$.

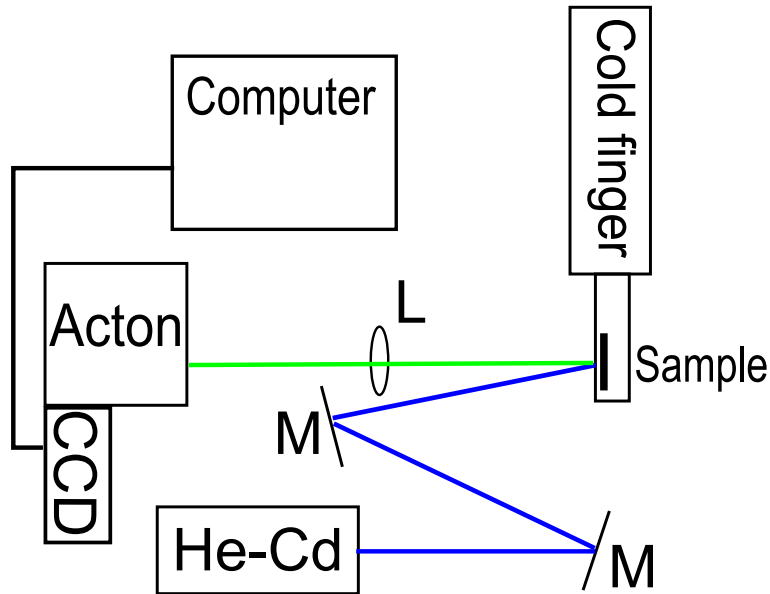


Figure 5.10: Cold finger setup for investigation of the spectral temperature dependence of samples. A HeCd laser @325 nm were used as excitation and two guiding mirrors(M) directs the beam onto the sample. Fluorescence from the sample are collected by a lens(L) and focused onto a spectrometer(Acton). The spectrum is detected by CCD camera and recorded on a computer.

and thereby the photo induced damage to the sample.

After the spectrum at 5 K was taken the sample was gradually heated back to room temperature stopping at intermediate temperatures to record a spectrum.

5.4 EPI-fluorescence microscope

Besides the Epi-fluorescence part of the LSM a Nikon Eclipse ME600D EPI-fluorescence microscope with a Hg excitation source centered at 365 nm was used for several purposes with the investigated nanostructures:

- Fluorescence spectra of the nanostructures were recorded with a fiber spectrometer (Ocean optics model:Maya)
- Fluorescence images with a mounted CCD camera for investigation of morphology, polarization and waveguiding characteristics.

5.5 SEM

The scanning electron microscope (SEM) images in this thesis were made using a Hitachi S-4800 Field Emission Scanning Electron Microscope which allows for imaging with very low acceleration voltage. Since the investigated nanostructures are non-conducting and the molecular bonding is primarily of Van der Waals type the low acceleration voltage is necessary: otherwise charging effects will damage the samples. To enhance image quality and to further minimize charging effects the samples were coated with 3 nm of a Au/Pd mixture with a Cressington 208HR sputter coater. SEM images were used to investigate the morphology of the fabricated organic nanostructures.

Chapter 6

Organic 1D nanostructures

This chapter will describe two different types of organic 1D nanostructures, both are made by bottom-up methods and the end result is mass fabrication of 1D nanostructures. The two systems are: 1) the thoroughly investigated and characterized surface grown para-phenylene nanofibers [16, 17, 8, 18, 19, 20, 21, 22, 6, 7, 9, 11] and 2) template assisted grown nanotubes of a small novel molecule called Tbf (Tetrabenzofluoren). The first will act as a reference and benchmark system for comparing the performance of the second system. Both of the investigated systems are so-called molecular crystals and the nanostructures will therefore inherit many of their characteristics from the individual building blocks of the crystal. With this in mind the description of each system will start with the properties of the individual molecular unit and then proceed with characteristics and parameters of the nanostructure itself. The description will be rounded off with functionalization of both kind of nanostructures, either by changing the molecular unit or by incorporating them in core shell structures, both done in order to tailor the nanostructures to specific purposes. In the next chapters optical properties of the nanostructures will be investigated and characterized for a more complete description.

6.1 Surface grown para-phenylene nanoaggregates

6.1.1 Introduction

In the last decade it has been demonstrated in numerous articles the possibility of growing mutually aligned single crystalline nanofibers from small molecules of the conjugated oligomer family; para-phenylenes on a variety of substrates and by different growth techniques [16, 17, 8, 18, 19]. The interest in para-phenylene 1D nanostructures stems from their very interesting optical properties like anisotropic emission characteristics with high quantum yield [16, 20, 21], well defined emission spectra in the visible spectral range [22], waveguiding [6, 7, 8, 9] and random lasing [11]. These optical

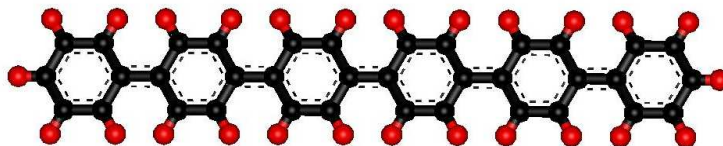


Figure 6.1: Single p-6P molecule shown in a completely planar configuration, i.e. the torsion angles are 0° . The length of a single p-6P molecule along the backbone is 2.44 nm , which also defines the direction of the molecular axis.

properties makes para-phenylene nanofibers interesting for application as fluorescent markers, in electronic and optical devices[23] and in nanowire-transistors[24].

In this section I will describe surface grown para-phenylene nanofibers and their characteristics by describing the example para-hexaphenylene(p-6P) grown by OMBE(Organic Molecular Beam Epitaxy) on a mica substrate.

6.1.2 The molecular unit

The p-6P molecule ($C_{36}H_{26}$) is an aromatic compound consisting of six phenyl rings in para configuration which make the molecule rod-like as seen in figure 6.1. An isolated p-6P molecule will not have a planar configuration as shown in the figure but will rather have torsion angles ranging from 40° to 47° between adjacent phenyl rings[25]. The degree of torsion originates from two opposing forces; the intramolecular repulsion between ortho-hydrogen atoms from different phenyl rings which will tend to make the torsion angle larger and the π -electron system, which will drive the molecule towards a more planar configuration due to resonance interaction. When the p-6P molecule becomes part of a crystal environment interchain interactions, i.e. packing forces drive a further planarization of the molecule and the torsion angle becomes significantly smaller[26, 27, 28].

6.1.3 Para-hexaphenylene in the solid phase

Para-hexaphenylene molecules crystallize in a monoclinic lattice with-in the space group $P2_1/c$ with lattice constants; $a=26.264\text{ \AA}$, $b=5.565\text{ \AA}$, $c=8.091\text{ \AA}$ and $\beta=98.17^\circ$ [29, 30]. The crystal structure is of the herringbone type where the molecular axes are parallel and are characterized by a large tilt angle of 66° between adjacent molecule planes, as seen on the right side in figure 6.2. The individual molecular building blocks in one layer of the crystal phase are

held together by at least two different forces: Van der Waals interactions and Coulomb forces. The former is relatively weak and decreases rapidly with increasing distance as: $F_{Van\ der\ Waals} \propto 1/r^6$, where r is the intermolecular distance and the interaction stems from dipoles created by fluctuations in the electronic configuration of the involved molecules. The Coulomb force, $F_{Coulomb} \propto 1/r^2$ is due to shift in the electronic configuration of the aromatic molecule by charge shifting from the hydrogen atoms to the carbon atoms. The Coulomb force will dominate the crystal packing, because it is the stronger of the two forces and will drive the long axes of the molecules to align parallel to each other creating a sheet structure with large tilt angle between adjacent molecules, i.e. herringbone structure[31, 29]. Interactions between different horizontal layers are of the Van der Waals type and are therefore weaker than the interactions within one layer.

When molecules are deposited on a substrate there is also an interaction between the surface and the molecules which will tend to direct molecules in the initial, i.e. primary layer on the surface; how much depends on the strength of the interaction[32]. Part of this interaction stems from substrate-overlayer epitaxy, i.e. how much the lattices of the substrate and overlayer are matching. The final structure of the overlayer will therefore be the result from the competition between the energy lowering of the epitaxy and the energy required for changing the lattice of the overlayer to that degree of epitaxy. Other interactions than epitaxy can influence the final way molecules position on the surface, as will be discussed in the next section.

6.1.4 p-6P on mica

The choice of using the sheet silicate Muscovite mica ($K_2Al_4[Si_6Al_2O_{20}](OH)_4$) as substrate stems from several reasons. First the lattice parameters of mica are very similar to the ones of p-6P; $a=5.2 \text{ \AA}$, $b=9.1 \text{ \AA}$, $c=19.7 \text{ \AA}$ and $\beta=95.78^\circ$ [19], so there will be a large degree of matching between the two lattices. Second the surface roughness of cleaved mica is only about 2 \AA over areas of several hundred of nanometers[33]. The third aspect is the strong surface dipoles which are created when mica is cleaved . In the cleaving process half of the K^+ ions , between two layers of Si-O are removed leaving the remaining K^+ ions to form dipoles with an equal number of Al^{3+} ions[34]. The dipole axis is rotated 15° with respect to the unit vectors[16] and plays a crucial role in the formation of the initial layer which is seen in figure 6.3.

The surface dipoles interacts with initial layer of molecules through dipole field-induced dipole interaction since p-6P molecules do not possess any permanent dipole moment. The induced dipole moment of the molecules will be along the long molecule axes and this axis will therefore align itself parallel to the surface dipole direction. The strength of the interaction depends on the polarizability of the molecule and the field strength of the

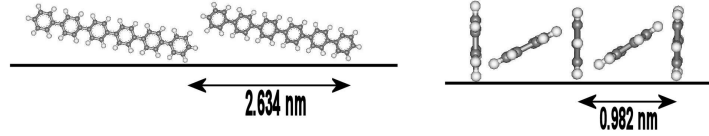


Figure 6.2: On the left the parallel orientation of the p-6P molecule on a surface. Two molecules are shown in a side view tilted about 4.5° against a surface, this is the angle which p-6P makes with the surface when mica is used as a substrate and the fabrication parameters are optimized. On the right five molecules are shown in a parallel view along the molecular planes with a tilt angle of 66° .

surface dipoles and is given by:

$$W \approx \frac{\alpha_0^2 E^2}{R^3} \quad (6.1)$$

where $R \approx 3.5 \text{ \AA}$ is the optimum distance between neighboring surface molecules given by the van der Waals radii[30], $E = 10^7 \text{ V/cm}$ is the strength of the surface dipoles[35] and the polarizability α_0 of the molecule is given by the Lorenz-Lorentz equation:

$$\frac{\alpha_0}{4\pi\epsilon_0} = \left(\frac{n^2 - 1}{n^2 + 2}\right) \frac{3M}{4\pi N_0 \rho} \quad (6.2)$$

When the following values are used for the refractive index $n=1.62$ for p-6P [36], Avogadro's number $N_0=6.022 \cdot 10^{23} \text{ mole}^{-1}$, the mass of the molecule $M = 458 \cdot 10^{-3} \text{ kg/mole}$ and the density $\rho=1,2 \cdot 10^3 \text{ kg/m}^3$, then a value results of $\alpha_0 \approx 56 \text{ \AA}$. With this value for the polarizability equation 6.1 gives an interaction energy of $W \approx 51 \text{ meV}$ which is larger than the thermal energy of molecules at the surface ($W_{thermal} = k_b T \approx 28 \text{ meV}$ when $T = 50^\circ \text{C}$) so the excess energy can be used to orient molecules on the surface[16]. This together with the point-to-line coincidence epitaxy between the mica and the molecules drives the growth process in the initial stage. Beyond this intermolecular forces are the dominant driving force. The above calculations are only valid for laying molecules on the surface, like seen on the left in figure6.2.

6.1.5 Fabrication of para-phenylene nanoaggregates on mica

Since sample preparation of para-hexaphenylene nanoaggregates has not been an integrated part of this project, this section will be a brief summary of the process and important parameters. If the reader are interested in a more elaborated explanation of the process it can be found in [16, 37]

In order to fabricate high quality nanoaggregates, control of four growth parameters are important and will influence the result of the final sample, the four parameters are:

1. Substrate temperature: The most important of the growth parameters to control since there is only a small temperature interval of $\pm 15 K$ around $T_{optimal}$ where long mutually aligned nanoaggregates are formed on the mica surface. I use $T_{optimal}$ here because the value is dependent on where on the sample holder or sample it is measured during the growth process, so it is setup dependable in contrast to the temperature interval which is not. At room temperature closed films of standing molecules are formed, at elevated temperatures but still below the optimal temperature small islands are formed and above the optimal temperature island formation is again observed. Finally at high temperatures the molecules desorb from the substrate.
2. Deposition rate: The optimal deposition rate is $0.1 \text{ \AA} / \text{s}$ [34] and above $0.5 \text{ \AA} / \text{s}$ the molecules will tend to stick together and therefore not find their optimum position on the substrate inducing defects in the nanoaggregate.
3. Base pressure of the chamber: The base pressure should be kept as low as possible during the growth process, if it raises above $\approx 10^{-6}$ mbar impurities are incorporated into the nanoaggregates creating defects.
4. Final nominal thickness of the overlayer: Controls the final dimensions of the fabricated nanoaggregates together with the substrate temperature.

If the four growth parameters are adjusted right nearly defect free well aligned single crystalline nanoaggregates are fabricated on the mica surface as seen on the left in figure 6.3. Typical height and width dimensions of para-hexaphenylene nanoaggregates are from a few tens to a couple of hundred nanometers while the lengths can be up to 1 μm giving the nanoaggregates a large aspect ratio. On the right in figure 6.3 it is seen how the individual molecules are aligned in the nanoaggregate which will have a large influence on the optical properties which will be described in the optics part of this thesis.

In the fabrication process it is also possible to tailor properties of the surface grown nanoaggregates by changing the individual molecular building

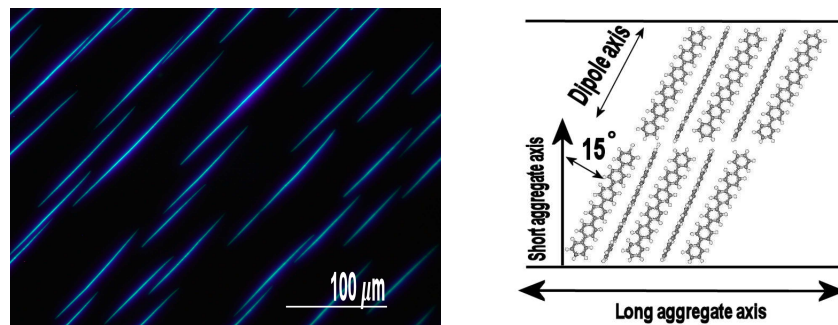


Figure 6.3: Left: Epifluorescence image of para-hexaphenylene nanoaggregates on mica. Right: Orientation of the para-hexaphenylene molecules in the fabricated nanoaggregates. There is a 15° angle between the the short axis of the aggregate and the long molecular axes which are parallel to the surface dipoles[38]

block. This induces a change of structure geometry and optical emission characteristics[39]. Functionalized surface grown nanoaggregates will not be investigated further in this thesis.

6.2 Template assisted grown nanostructures

6.2.1 Introduction

In the last years there has been an intensive investigation into the template-based synthesis of nanostructures because of the methods availability and the resulting ability to fabricate free-standing arrays of nanostructures which are desirable for new and effective photovoltaic cells and luminescent diodes[40, 41]. This method for mass fabrication of 1D nanostructures uses a structured template in which material is deposited so the shape and dimensions of the nanoaggregates are dictated by the template. The principle is very general and has been used to process materials ranging from metals to polymers[42, 43, 44, 45, 46, 47].

In this section I will introduce an example of template assisted grown nanostructures of a small organic molecule and a cleaning method in order to produce individual nanostructures, which are the interest of this project.

6.2.2 The molecular units and crystals

Tbf or 17H-Tetrabenz[a,c,g,i]fluoren is a small symmetric organic compound, which looks a little like a butterfly and is seen in a planar configuration on the left in figure 6.4. On the right in the same figure a substituted

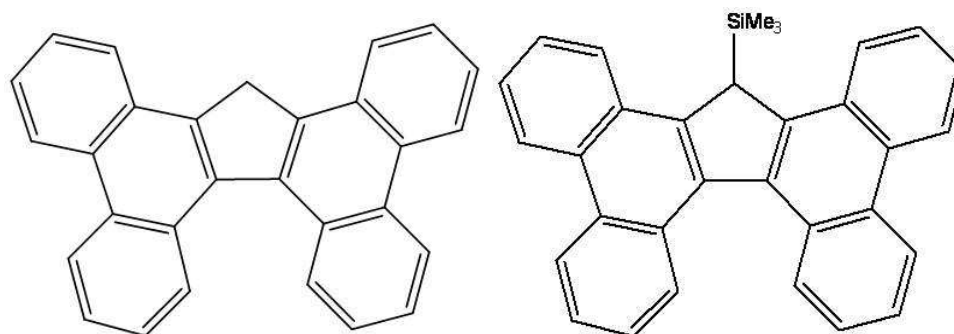


Figure 6.4: Left: Single Tbf (17H-Tetrabenzofluorene) molecule in a planar configuration[48]. Right: Single Tms-tbf (17-Trimethylsilyltetrabenzofluorene) molecule in a planar configuration[48].

version of the Tbf molecule called Tms-tbf are shown. In this project both of the molecules has been used as materials for 1D nanostructures but also in combination in core shell structures.

As with the p-6P molecule an isolated Tbf or Tms-tbf molecule will not be planar, as shown in figure 6.4 but will be in a twisted configuration where the "wings" of the butterfly will flip back and forth[48, 49]. When the molecules pack in the crystal phase the flipping stops and the molecules aligns in a face to face configuration in the "a" direction of the crystal seen on the left in figure 6.5. In this configuration there will be a large overlap of the π -electron system of the molecules. In the crystal "b" direction the face to face stacks of molecules will arrange in a herring bone structure seen on the right in figure 6.5. This packing is for the Tbf monoclinic crystal and will maybe not be valid for the fabricated nanostructures because of the usual polycrystalline nature of template-based growth[50].

6.2.3 Templates

The driving force in template-based methods is the surface energy of the pore walls and of the deposited material which will determine if rods or tubes are produced [51]. Organic materials and most polymers are considered as low-energy materials with respect to their surface energies so they will spread quickly on a high energy surface creating a film of material[52]. Because the pore has a finite area the strong adhesive forces are neutralized after the formation of the precursor film and the weaker cohesive forces will drive the complete fill of the pore and therefore a longer fabrication time has to be used if rods are the desired structure.

The most commonly used templates are anodized alumina membranes

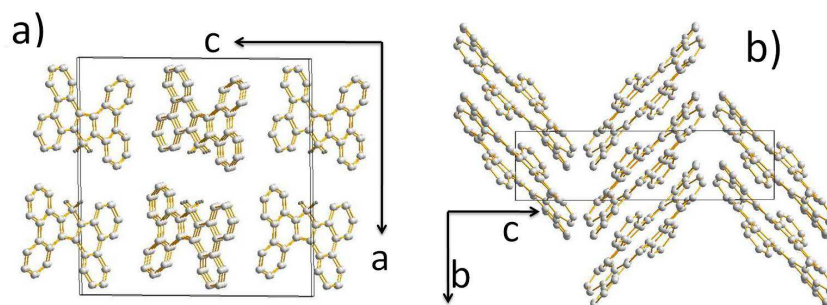


Figure 6.5: Tbf single crystal seen along two different crystal directions. a): Tbf single crystal seen along the b direction of the crystal, here the face to face packing of the molecules are seen[48]. b): Tbf crystal seen along the a direction of the crystal, here the herringbone packing is clearly seen[48].

(AAM) but a large number of materials can be processed and used as templates for structure fabrication. There are however some general criteria that the chosen material should fulfill. The template material should be chemically and thermally stable during the synthesis and the following process steps [50]. Commercial purchased AAO (anodized aluminaoxid) membranes from "Whatman Inc." were chosen as template material for the structures investigated in this thesis. They were chosen because they meet the stability requirements and they are available with specific pore size, pore size distribution, porosity and they have a high surface energy. The templates used had pore diameters of either 100 or 200nm and a thickness of $60\mu\text{m}$ giving the fabricated nanostructures an aspect ratio of 300:1 or 600:1.

The problem with using AAM is to achieve a complete removal of the template with wet chemical etching. This problem will be addressed in a separate section later in this chapter.

6.2.4 Fabrication method

There are several methods with which material can be deposited in the template. It can be done either from a solution[52], by electro chemical deposition[50], by physical vapor deposition[53] or from a melt[46]. The investigated nanostructures in this thesis are made by the melt method where the material is placed on top of the template and then heated to well above the single crystalline melting temperature in an oven with a protective argon atmosphere. The material and template are heated for a specific period of time and then cooled to solidify the structure inside the template. If the reader wishes for a more elaborated description of the fabrication process and growth parameters it can be found in[54, 55] but

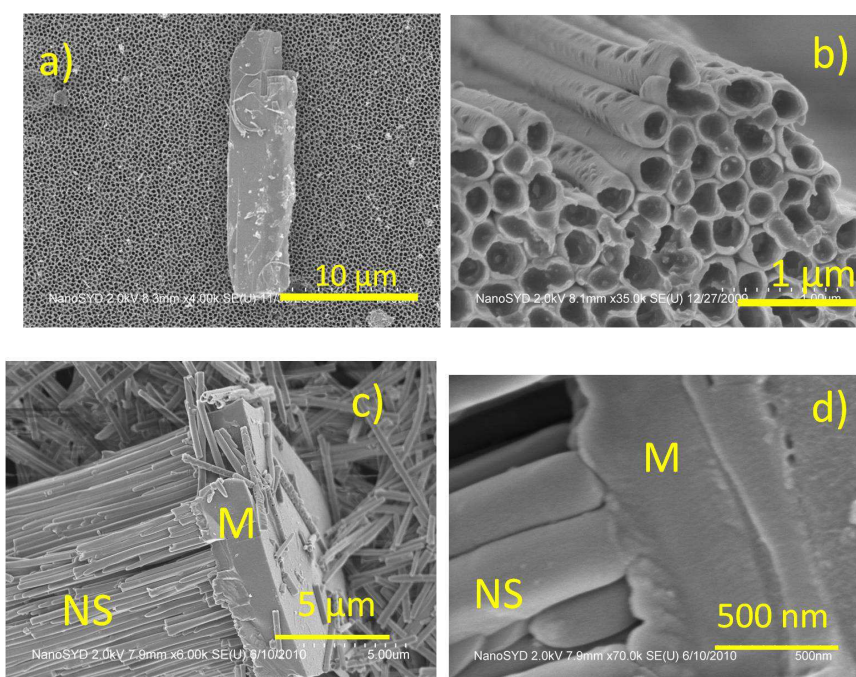


Figure 6.6: a) SEM image of a TbF single crystal on top of a porous alumina template. b) SEM image of TbF nanotubes fabricated by template-based molecular melt process. c) and d) shows SEM images how the molten material(M) deposited on the template forms the nanostructures(NS) by flowing into the pores of the template. In image b), c) and d) the template has been removed by wet-chemical etching and all samples are sputter coated with 3nm Au-Pd for SEM imaging

will not be discussed further in this project.

In figure 6.6 SEM images are shown the different steps in the fabrication process. Image a) show a single TbF crystal placed on the template before the melting process and image b) the fabricated nanotubes after the AAO template has been removed. Images c) and d) shows how the molten material from the template top forms the nanostructures during the process. In images b), c) and d) the templates has been removed by wet-chemical etching.

The core shell structures, which are also investigated in this project, are also made by the melt method but in a two step process. The outer shell are fabricated first by the same process as described above after which material residue is removed from the template. Then a second melting process is made but now the pores has a low surface energy because of the precursor film so the second step will have a longer process time than the first step.

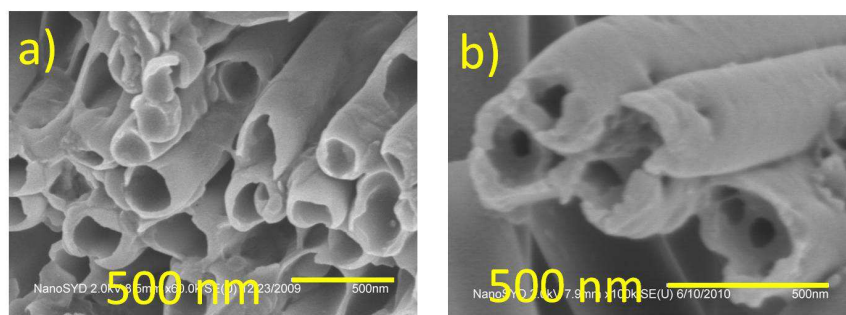


Figure 6.7: a) SEM image of TbF nanostructures. b) SEM images of core-shell structure with TbF shell material and Tms-tbF as core material.

In figure 6.7 SEM images of TbF nanostructures and core-shell structures made of TbF as wall material and Tms-tbF as core material are shown for comparison. Because the two different materials in the core-shell structure are very similar no contrast can be seen between them in the SEM image.

6.2.5 Template removal

Releasing the 1D nanostructures from the AAO template requires either destruction of the template by wet-chemical etching or a method to "pull" the structures out of the template. The second process is done by a soft lift-off process where the material melt on top of the template is glued to a stud and the underside of the template is glued to another stud. The two studs are then pulled apart with the nanostructures attached to the top stud. This process is very sensitive to lateral forces under the separation process and on the adhesion between the nanostructure and the template [51]. To increase the yield of this process one can minimize the adhesion between the template wall and the material by lowering of the surface energy of the template wall. This has the unfortunately effect that tubes no longer are fabricated but rods, because the process goes from having a wetting layer in the high-energy pores to a simple pore filling in the low-energy case. Furthermore this technique has only been done on structures which have a maximum aspect ratio of 10:1 and a diameter of 500 nm and under optimized conditions. The nanostructures described in this project has a aspect ration as large as 600:1 so this process is not an option in our case. We therefore chose to wet-chemical etch the AAO templates.

For all of the samples the wet-chemical etching was done with a 10 per cent NaOH solution. For optical characterization of the nanostructures the template should be fully dissolved so the template or templates were immersed in the NaOH solution and left for 24 hours giving a solution like the one seen in upper left corner of figure 6.8. In the optical characterization

chapters there are investigations of this solution but if nanostructures has to be used in applications the residues from the wet-chemical etching of the template has to be removed. The chosen cleaning technique was to filter the solution with a nylon membrane filter with a 450nm pore size. The filter was placed in the setup seen in the lower left corner of figure 6.8 and the solution was poured onto the filter as seen in the upper right corner of the same figure. The filter was then rinsed with DI water until the PH reached a value of 7 indicating that more or less all of the NaOH was removed ending up with a filter as seen in the lower right corner of figure 6.8. The brown coloration of the filter stems from the AAO template which gets a brownish color when heated to the fabrication temperature.

After the filtering process the filter was inspected in the fluorescence microscope to check if there were any nanostructures retained by the filter as seen in figure 6.9. The Tbf nanostructures in the figure seems to be non-fluorescent this issue will be discussed in the optical characterization section of the thesis. Bundling of the nanostructures after template removal is a general problem which is due to both capillary forces between adjacent nanostructures which will cause them to stick together[41] and molten material which has not gone into the template pores but solidified on top of the template making the nanostructures stick together in one end.

The filter is then put in a glass vial filled with DI water and sonicated for a short period to lift the nanostructures from the filter. The filter is then removed from the solution leaving the nanostructures suspended in DI water ready to be drop casted on a substrate for optical characterization. The filtered solution unfortunately does not only contains nanostructures but also small non-dissolved fragments of the AAO template, this does not in general pose a problem in the optical characterization of individual structures but if the process has to be up-scaled another cleaning step, for instance separation by centrifugation has to be done.

A second and slightly different method of wet-etching was used for partial removal of the template. In this method a filled template was mounted on a SEM stub with a carbon pad and a few drops of the 10 per cent NaOH solution was added on top and left for half an hour. Then the partly desolved template was rinsed in DI water and sputter coated with 3nm Au-Pd for SEM imaging. The method was developed to fix the fabricated structures in order to study the general morphology before the optical characterization was conducted. In figure 6.10 Tbf nanostructures inside a partly removed template are shown where the smoothness and tube like structure are seen.

6.3 Summary

In this chapter, two different methods for fabrication of 1D nanostructures have been presented from the individual molecular unit to how they assemble

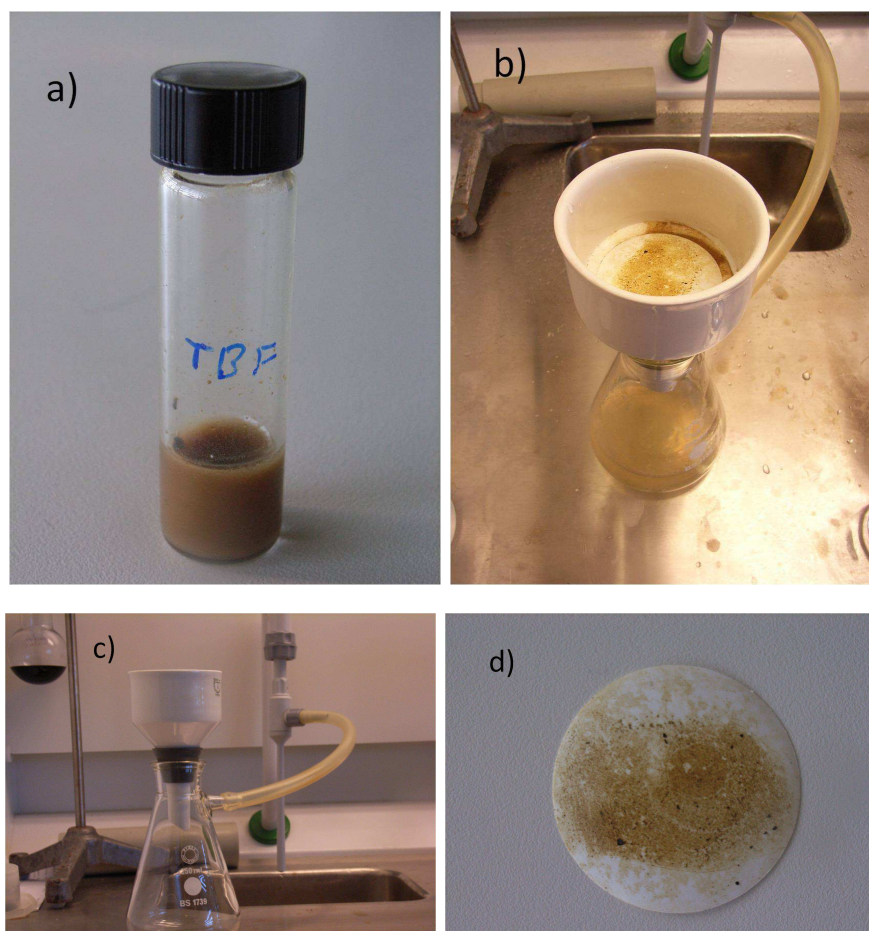


Figure 6.8: a) Dissolved TbF₃ filled AAO templates in NaOH. b) The solution dispersed on the filter. c) Filter unit setup. d) The filter after the cleaning procedure. The filter has a diameter of 47 mm.

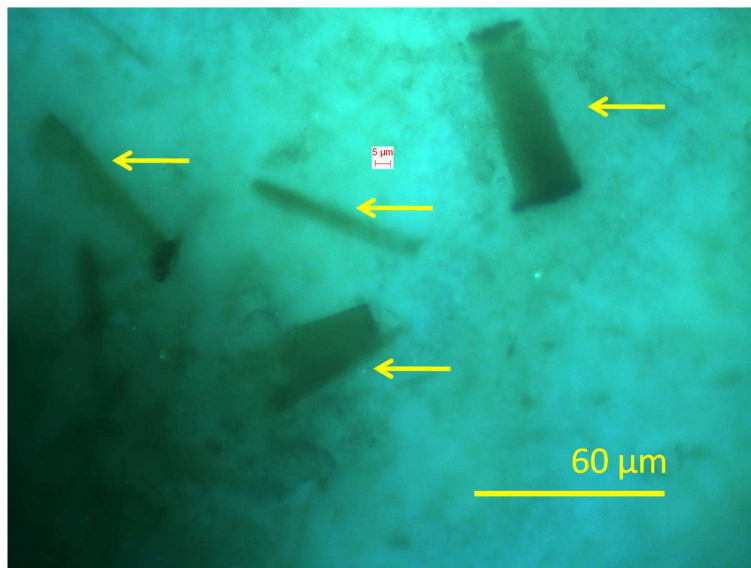


Figure 6.9: Epi-fluorescent image of the nylon filter with bundles of non-fluorescent Tbf nanostructures. The nanostructures are $60\mu\text{m}$ long the same length as the thickness of the AAO template indicating that the material wets the full length of the template pores. The bundles are marked with yellow arrows in the image.

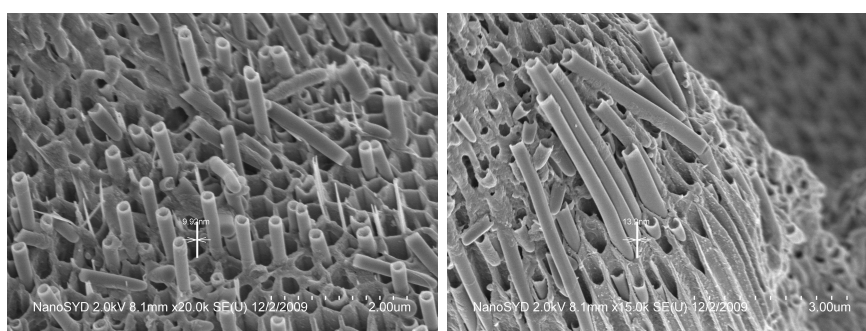


Figure 6.10: SEM images of Tbf nanotubes inside a partial removed porous alumina template.

into the finished structures. Both methods produces structures with a high aspect ratio but the two methods have advantages and disadvantages.

The surface grown para-hexaphenylene system offers a large degree of control over the growth process and the final structures are well defined and highly crystalline. The down side is that the fabrication process is done in ultra high vacuum (UHV) and is difficult to upscale.

The template assisted system does not offer the same degree of control of the growth process and the final nanostructures are usually polycrystalline. The fabrication process is faster and does not take place in UHV but this method needs additional cleaning steps in order to isolate the nanostructures. This method is easy to upscale but consumption of templates is one drawback that could prevent an upscaling of the method [51].

Chapter 7

Linear optical characterization

7.1 Introduction

In this chapter the linear optical response of both the starting materials and the nanoaggregates will be investigated. For a general introduction into the optical response of organic molecules see for instance[56, 57, 58]

The main focus of this chapter lies on temperature dependent steady-state linear spectroscopy. This is triggered by the observation that cooling para-hexaphenylene nanofibers reveals details about their morphology, more specifically about their polymorphism and phase transitions[59, 60]. The low temperature investigation is carried out on both types of nanostructures and on the molecular materials prior to fabrication. Before the low temperature characterization there will be a brief discussion about room temperature observations of samples with materials for the template assisted growth method and the nanostructures fabricated by this method. The last part of the chapter will discuss the observation of non-fluorescent nanotubes.

7.2 Room temperature observations

For comparison with low temperature spectra room temperature spectroscopy were conducted on samples with starting materials for the template assisted growth method and nanostructures from this method. Both starting material and nanostructures were drop casted on microscope slides and spectra were made with a fiber coupled spectrometer(Ocean optics: Maya) which were mounted as detector on the Nikon Eclipse ME600D EPI-fluorescence microscope as seen on the left in figure 8.2. In figure 7.1 spectra of the two starting materials, 17-Tbf and 17-Tms-tbf for the template assisted nanostructures are shown together with the spectra of the molecular material 8-b-H-Tbf from which Tbf is produced by pyrolysis. In figure 7.2 fluores-

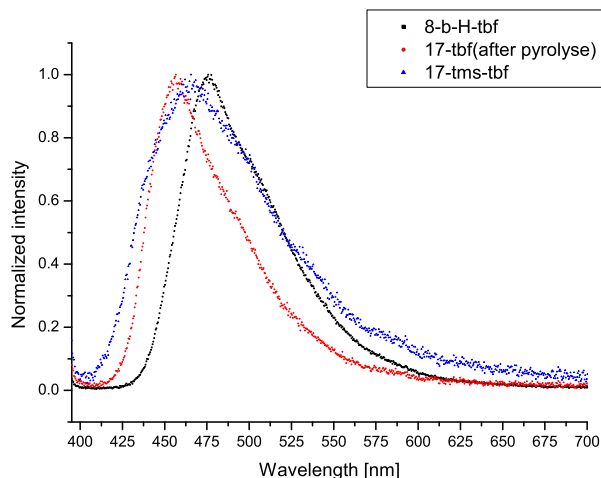


Figure 7.1: Normalized fluorescence spectra of 8-b-H-Tbf, 17-H-Tbf and 17-Tms-tbf at room temperature. The maximum intensities in the spectra are at 474.61 nm for 8-b-H-Tbf, 453.63 nm for 17-Tbf and 465.71 nm for 17-Tms-tbf. Only for the Tms-tbf spectra does the position of the maximum intensity not coincide with the position of the fitted peaks, see tables 7.1, 7.2 and 7.3 for fitted peak positions.

Table 7.1: Fitting values for 8-b-H-Tbf

8-b-H-Tbf	peak position [nm]	Width(FWHM) [nm]	Ratio
(0-1)	474.61	38.12	1
(0-2)	509.87	40.03	0.525
(0-3)	548.0	70.53	0.168

cence images of the three materials are shown and the crystalline nature of 8-b-H-Tbf, 17-H-Tbf are seen while the structure for 17-Tms-tbf seems to be less well defined. The fluorescence color of the materials gives a good indication about the main peak position but analysis of the spectra were done by fitting the spectra with Gaussian shaped peaks in the computer program PeakFit where peak position, width of the fitted peaks and amplitudes were found. Fitting values for the different spectra are given in the tables 7.1, 7.2 and 7.3. In the tables I have assumed that the (0-0) transition is absent in the spectra due to self-absorption and the first peak in the fitting is therefore assumed to be the (0-1) transition.

In figure 7.3 fluorescence spectra of 17-H-Tbf and Tms-tbf nanostructures are shown. They are fitted in the same way as described above and



Figure 7.2: Fluorescence images of 8-b-H-Tbf, 17-H-Tbf and 17-Tms-tbf. Both 8-b-H-Tbf and 17-H-Tbf seems to have a well defined crystalline structures while 17-Tms-tbf seems to be less well defined.

Table 7.2: Fitting values for 17-H-Tbf

17-H-Tbf	peak position [nm]	Width(FWHM) [nm]	Ratio
(0-1)	453.63	31.61	1
(0-2)	478.42	41.94	0.605
(0-3)	510.83	40.99	0.332
(0-4)	544.19	40.99	0.130

Table 7.3: Fitting values for Tms-Tbf

Tms-Tbf	peak position [nm]	Width(FWHM) [nm]	Ratio
(0-1)	452.68	45.75	1
(0-2)	486.04	43.84	0.687
(0-3)	519.41	47.66	0.397
(0-4)	563.25	70.54	0.200

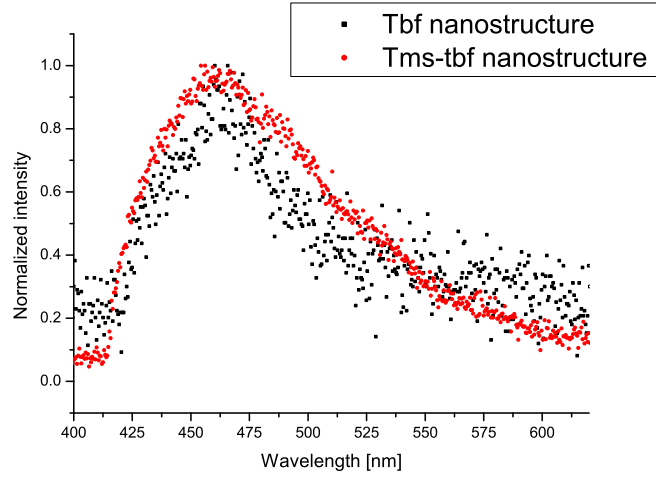


Figure 7.3: Normalized fluorescence spectra of nanotubes of 17-H-Tbf and Tms-tbf. The maximum intensities in the spectra are at 463 nm for both 17-H-Tbf and Tms-tbf.

Table 7.4: Fitting values for 17-H-Tbf nanostructures

Tms-Tbf	peak position [nm]	Width(FWHM) [nm]	Ratio
(0-0)	434.57	20.97	0.462
(0-1)	462.21	40.03	1
(0-2)	495.58	36.22	0.410
(0-3)	530.84	40.03	0.321
(0-4)	571.83	41.94	0.304

the fitting values are given in tables 7.4 and 7.5. From the fitting it was found that the spectra of the nanostructures have a contribution from a even higher energy peak than the starting materials, this contribution was said to come from the (0-0) transition. The fluorescence intensities of the nanostructures are very low making the signal to noise ratio of the experiments low and could influence the accuracy of the fitting. Maximum intensities in the spectra are at 463 nm for both 17-H-Tbf and Tms-tbf in good agreement with the largest peak amplitude in the fitting, but differs from the main peak position of the starting material.

Table 7.5: Fitting values for Tms-tbf nanostructures

Tms-Tbf	peak position [nm]	Width(FWHM) [nm]	Ratio
(0-0)	436.48	20.97	0.438
(0-1)	463.17	42.58	1
(0-2)	497.48	40.03	0.577
(0-3)	536.56	55.28	0.460

7.3 Low temperature spectroscopy

7.3.1 Introduction

The temperature dependence of the spectra has been investigated by cooling the samples down to a few Kelvin and then gradually heating them up again and taking spectra at fixed temperature intervals as described in the instrumental chapter. Cooling the sample has several effects, first the individual peaks in the spectra become better defined since the line width usually is decreasing. Second, cooling might reveal additional peaks if temperature dependent phase transitions occur. Third, the relative intensity ratio between the peaks change since the Huang Rhys factor changes. The Huang-Rhys factor corresponds to the average number of phonons involved when the excited molecule relaxes from the ground state configuration to the new equilibrium configuration in the excited state, after the absorption of a photon[61]. The Huang Rhys factor S can be determined from the fractional intensity of the individual vibronic peaks by:

$$S = \frac{(I_{0 \rightarrow 1} + 2 * I_{0 \rightarrow 2} + 3 * I_{0 \rightarrow 3})}{I_{Total}} \quad (7.1)$$

Here $I_{0 n}, n = 1, 2$ and 3 are the emission intensities of the vibrational transitions and I_{Total} is the sum of all the vibrational intensities.

7.4 Spectra of para-hexaphenylene

7.4.1 Para-hexaphenylene in powder form

The temperature dependence of the starting material for p-6P nanofibers was investigated by drop casting p-6P powder on a small piece of Si wafer with ethanol. The p-6P powder is not soluble in ethanol but the step was necessary so the powder would stick to the Si wafer. In figure 7.4 steady-state photoluminescence(PL) spectra for p-6P powder at three selected temperatures are shown. From figure 7.4 it can be seen that the (0-0) transition is only present at low temperatures and is suppressed by self-absorption at

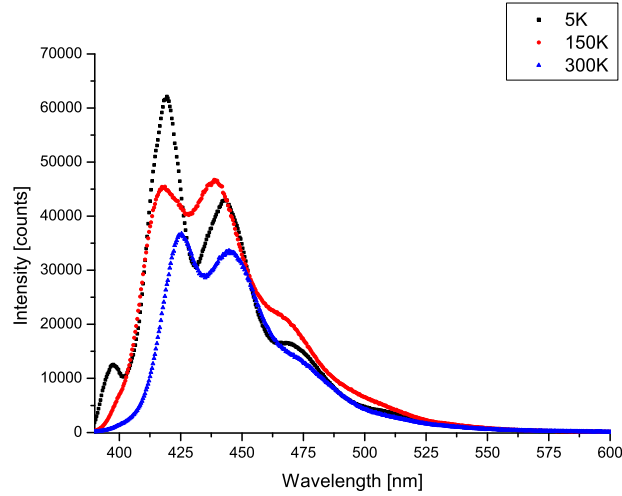


Figure 7.4: Low temperature spectra of para-hexaphenylene powder drop casted on a piece of Si wafer with ethanol. The excitation is @325 nm with an intensity of 4 mW/cm^2 and spectral resolution is 1 nm. The sample was cooled down to 5 K and then gradually heated.

temperatures above 100 K. These findings are in contrast to results found by Guha *et al.*[61] where the (0-0) peak was not observed at any temperature for p-6P powder. The difference between the two results could be the amount of powder on the sample. This is shown by another low temperature experiment conducted by the author of this thesis which shows that on a sample with a thicker layer of p-6P powder, the (0-0) transition was nearly not observable at temperatures below 100 K indicating the increased effect of self-absorption in thicker samples. The individual spectrum in figure 7.4 show a vibronic progression series of peaks indicating a coupling of the vibrations of the back bone to the electronic transitions. Using the computer program PeakFit each peak in the spectrum is fitted for each temperature and the temperature dependence of the individual peaks are investigated. From the fitting it is seen that the peak position of the (0-0) transition red shifts monotonous from 397 to 400 nm with increasing temperature. The three other fitted transition have a temperature dependence as seen for the (0-1) and the (0-2) transitions in figure 7.5. For these peaks the transitions are first blue shifted from 5 K to 150 K and then the transitions are red shifted from 150 K to 300K. This behavior is not observed in [61] where only a red shift is observed for all the transitions with increasing temperature. The Huang-Rhys factor S is calculated for the p-6P powder by equation 7.1 and the temperature dependence of the factor is shown in figure 7.6. The findings are in very good agreement with results found in[61].

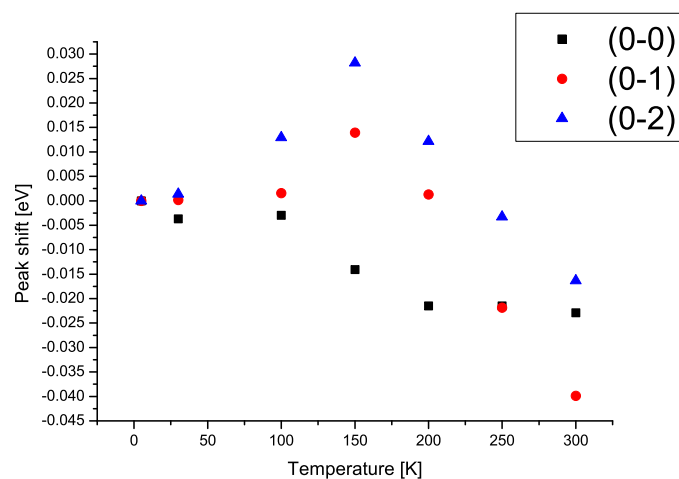


Figure 7.5: Temperature dependence of the three first transitions in p-6P powder.

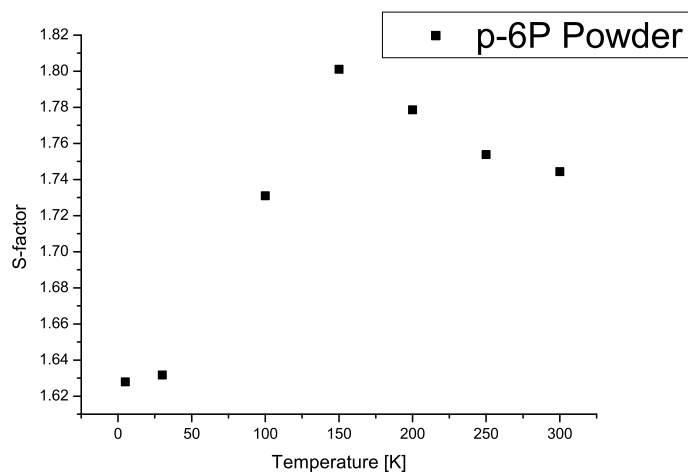


Figure 7.6: Huang-Rhys factor for p-6P powder versus temperature. S was calculated using equation 7.1

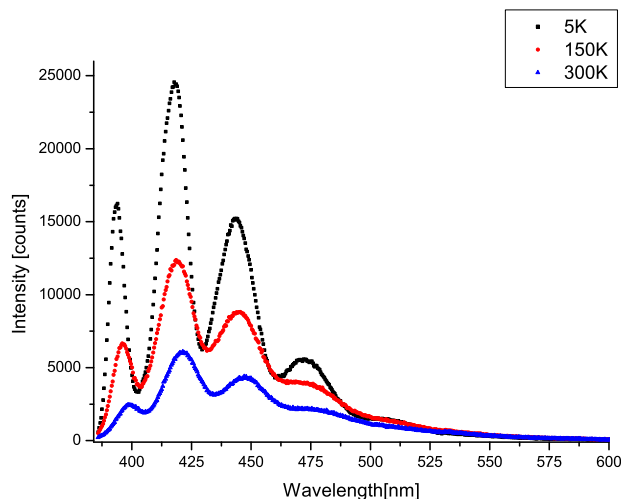


Figure 7.7: Low temperature spectra of para-hexaphenylene nanoaggregates on mica. The nominal thickness of the sample is 5 nm and the excitation is @325 nm with an intensity of 4 mW/cm² and spectral resolution is 1 nm.

7.4.2 Para-hexaphenylene nanoaggregates

In figure 7.7 steady-state PL spectra for p-6P nanofibers are shown at three selected temperatures. The individual spectrum in figure 7.7 show a vibronic progression series of peaks like for the p-6P powder. For the nanofibers all of the transitions are present for all temperatures and are again fitted by the PeakFit program. In figure 7.8 the temperature dependence of the three first transitions in p-6P nanofibers are shown and they are in perfect agreement with the results found in[59]. The Huang-Rhys factor as a function of temperature for p-6P nanofibers was calculated using equation 7.1 and is shown in figure 7.9. The p-6P nanofibers show a temperature dependence of the Huang-Rhys factor similar to results found in[61] for p-6P films.

7.5 Spectra of Tbf and Tms-tbf

7.5.1 Starting materials

The temperature dependence of the starting material for the template assisted grown nanostructures was investigated by drop casting the material on a small piece of Si wafer with ethanol. Both of the starting materials show a progression of vibronic peaks at low temperatures and a there are a gradual broadening of the peaks with increasing temperature as seen in figure 7.10 and in figure 7.13. The spectra are again fitted and the temperature dependence of the peak positions are seen in in figure 7.11 and in

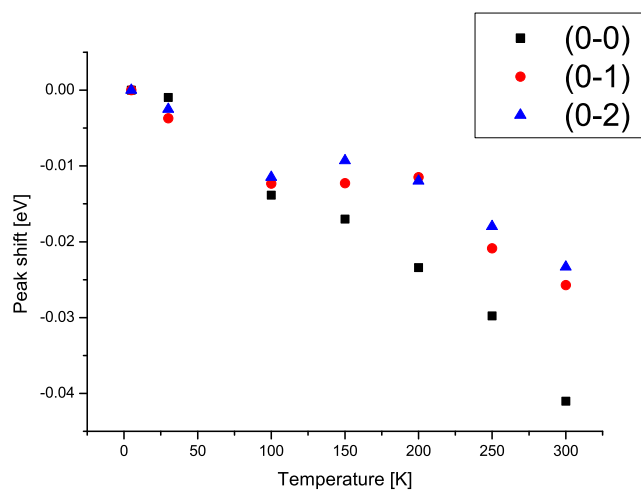


Figure 7.8: Temperature dependence of the three first transition in p-6P nanofibers.

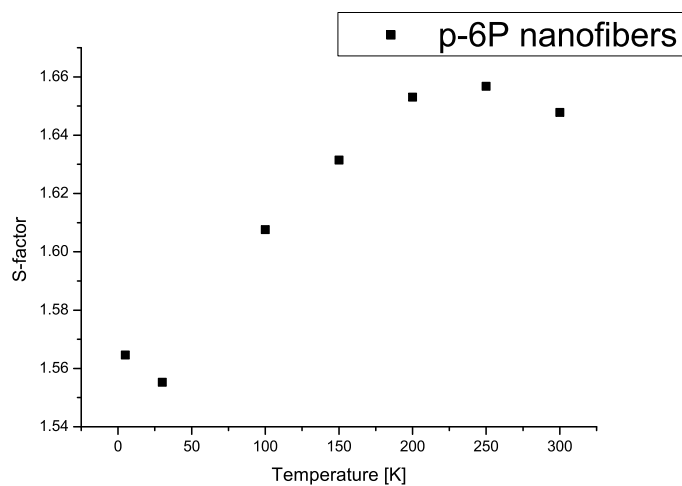


Figure 7.9: Huang-Rhys factor for p-6P nanofibers versus temperature. S was calculated using equation 7.1

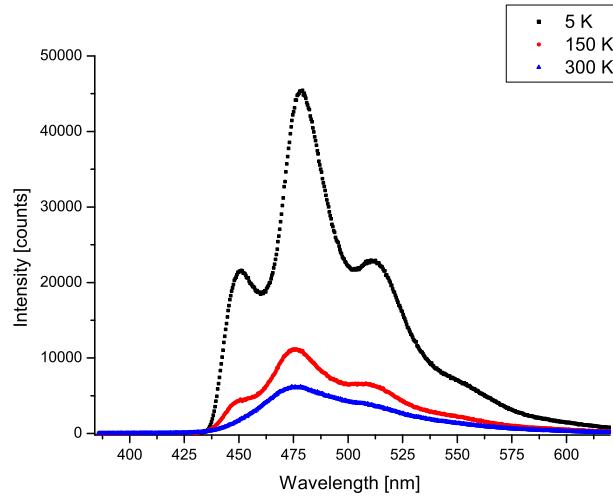


Figure 7.10: Low temperature spectra of tbf single crystals drop casted on a piece of Si wafer with ethanol. The excitation is @325 nm with an intensity of 4 mW/cm^2 and spectral resolution is 1 nm. The sample was cooled down to 5 K and then gradually heated.

figure 7.14. For Tbf crystals the peaks are first blue shifted from 5 K to 150 K and then red shifted from 150 K to 300 K like seen for the p-6P powder while for the Tms-tbf crystals a constant blue shift with increasing temperature was observed. The Huang-Rhys factor were calculated and Tbf shows a behavior like the one found for both p-6P powder and p-6P nanofibers seen in figure 7.12. Tms-tbf shows a not so well defined temperature dependence of the Huang-Rhys factor, as seen in figure 7.15

7.5.2 Spectra of nanoaggregates

Nanotubes fabricated from Tms-tbf were drop casted and investigated as described above, it was not possible to perform the investigation on Tbf nanotubes due to lack of fluorescence. At low temperature the spectrum of Tms-tbf nanotubes show vibronic peaks which broadens with increasing temperature and the spectrum becomes featureless at 300 K, as seen in figure 7.16. Fitting of the spectrum at 5 K identifies two additional high energy peaks not seen in the starting material of Tms-tbf. For a comparison the two spectra are normalized and plotted in figure 7.17 where it is seen that only the high energy tail of the spectra differs. From the fitting it is seen that these high energy peaks are present at all temperatures and the peak intensities are only weakly temperature dependent. These peaks are not contributed to the nanostructures and are therefore not part of the calculation of the Huang-Rhys factor for the nanostructures. All the

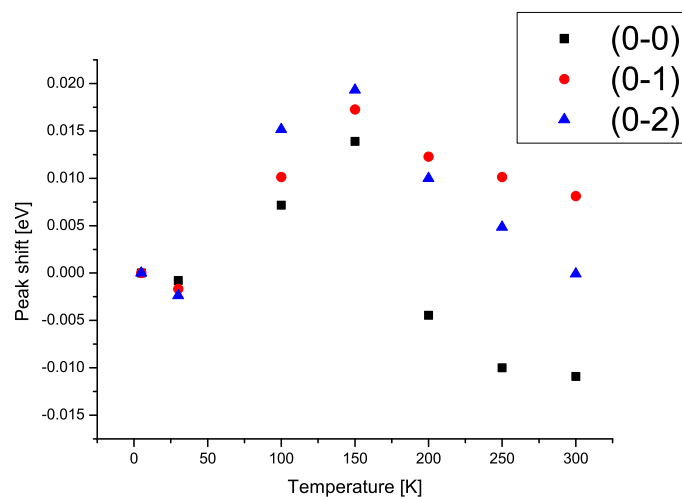


Figure 7.11: Temperature dependence of the first three transition in Tbf crystals.

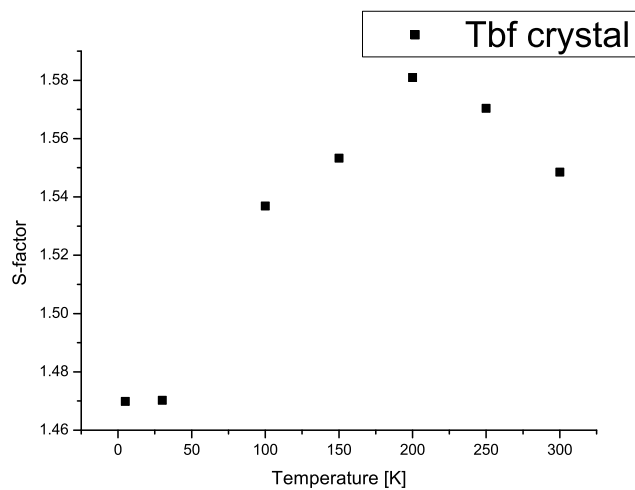


Figure 7.12: Huang-Rhys factor for Tbf crystals versus temperature. S was calculated using equation 7.1

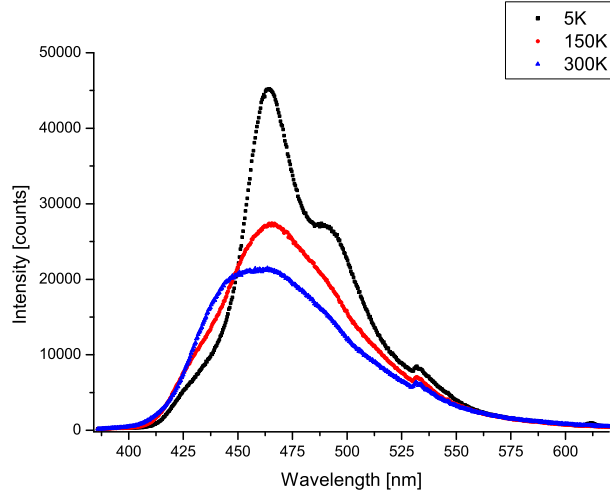


Figure 7.13: Low temperature spectra of tms-tbf single crystals drop casted on a piece of Si wafer with ethanol. The excitation is @325 nm with an intensity of 4 mW/cm^2 and spectral resolution is 1 nm. The sample was cooled down to 5 K and then gradually heated.

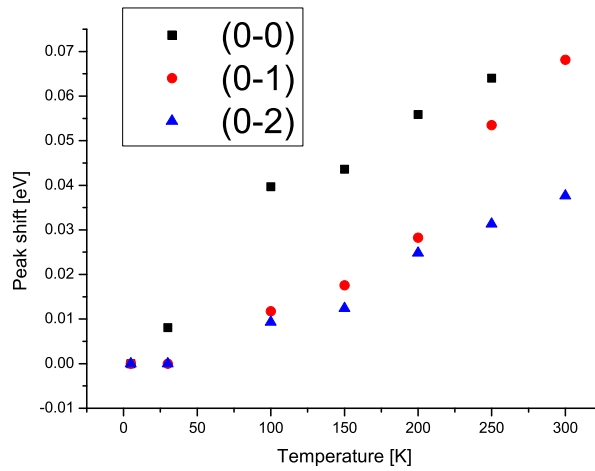


Figure 7.14: Temperature dependence of the first three transition in Tms-tbf crystals.

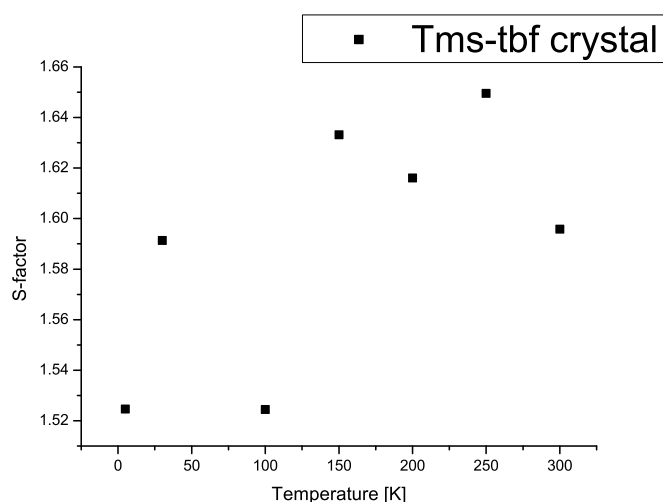


Figure 7.15: Huang-Rhys factor for Tms-tbf crystals versus temperature. S was calculated using equation 7.1

fitted peaks show are blue shifted with increasing temperature, as seen in figure 7.18 and resembles the behavior of the Tms-tbf starting material. The Huang-Rhys factor was calculated and is seen in figure 7.19 and is a behavior like the one found for the Tms-tbf starting material.

7.5.3 Core shell structures

Low temperature investigation of the fabricated core shell structures reveals a broad featureless spectrum for all temperatures, as seen in figure 7.20. The fluorescence intensity of sample are increasing with increasing temperature which could indicate aggregate states or chemical defects. The core shell structures were not further investigated.

7.6 Thermal decomposition

After removal of the AAO template by wet-chemical etching with NaOH the solution is drop casted on a glass slide and optical inspected. It is clear from figure 7.21 that there are many nanostructures but there is a huge difference between the optical properties of the fabricated nanostructures. This is illustrated in the images in figure 7.21 where on the left white transmission light is used for illumination and compared to images on the right where there is a combination of white transmission light and fluorescence excitation. All the nanostructures are fabricated in the same template so the optical properties are very sensitive to the fabrication process and template removal. It is seen in figure 7.21 that there are both fluorescent single

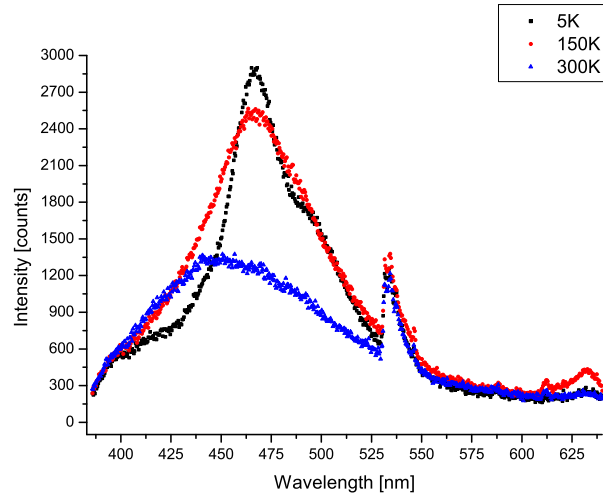


Figure 7.16: Low temperature spectra of tms-tbf nanotubes drop casted on a piece of Si wafer with ethanol. The excitation is @325 nm with an intensity of 4 mW/cm^2 and spectral resolution is 2 nm. The sample was cooled down to 5 K and then gradually heated. The artifact seen in the spectra @533 nm is a reflection from from the laser.

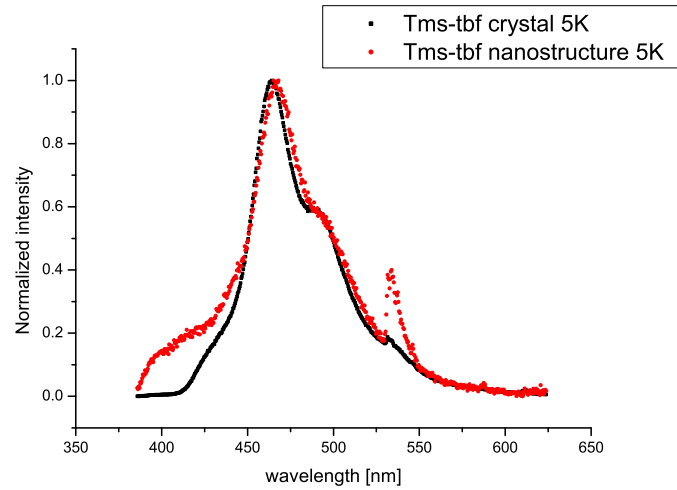


Figure 7.17: Comparison between normalized 5 K spectrum for the Tms-tbf starting material and the Tms-tbf nanostructures. The spectra are very similar but an additional high energy contributions are seen in the spectrum for the nanostructures.

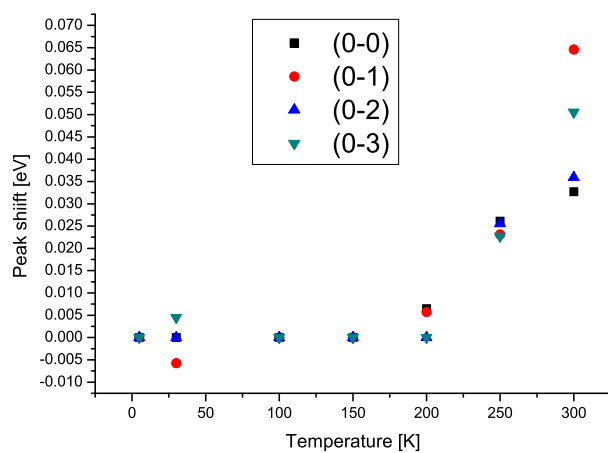


Figure 7.18: Temperature dependence of the first four transition in Tms-tbf nanostructures.

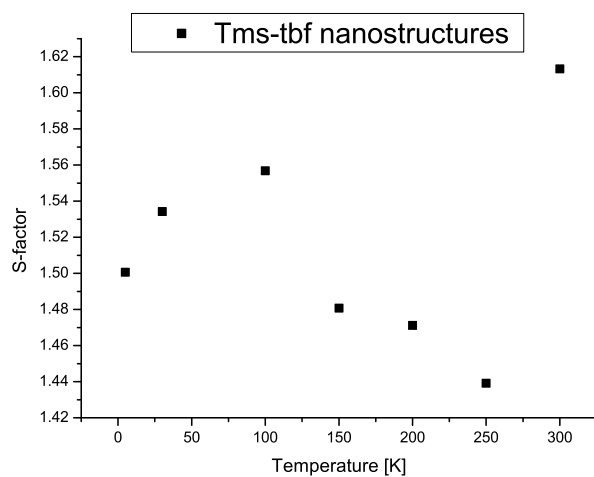


Figure 7.19: Huang-Rhys factor for Tbf crystals versus temperature. S was calculated using equation 7.1.

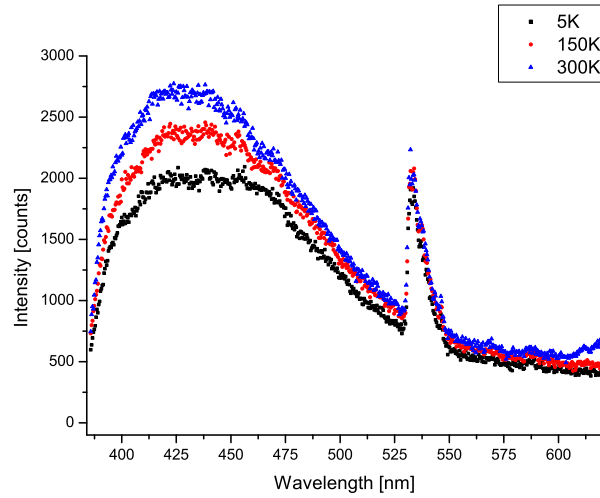


Figure 7.20: Low temperature spectra of tbf/tms-tbf core shell structures drop casted on a piece of Si wafer from a solution with DI water. The excitation is @325 nm with an intensity of 4 mW/cm^2 and spectral resolution is 2 nm. The sample was cooled down to 5 K and then gradually heated. The artifact seen in the spectra @533 nm is a reflection from the laser.

nanostructures and bundles of nanostructures but the opposite is also the case which means that nanostructure sticking together neither quenches nor inhibits fluorescence.

The difference in fluorescence emission from the nanostructures could stem from thermal decomposition of the molecules in the fabrication process, which are a known drawback of the melt process[62]. To test the thermal stability of the starting materials, powders of the both tbf and tms-tbf was placed on a glass slide and heated on a hotplate. Heating time and temperature resembles those of the fabrication process. The samples on the hotplate where heated in ambient air and not in a protective argon atmosphere as in the fabrication process, which will of course enhance oxidation of the samples. In figure 7.22 images of the heating experiment are shown. It is seen in b) that the Tbf crystal are nearly not molten at the fabrication temperature which will of course prevent the material from filling the pores of template but the material is still fluorescent. Heating the sample for an additional period of time with an elevated temperature melts the crystals but also induces a loss of fluorescence of the material as seen in c) and d). This could indicate that the material is either oxidized or thermally decomposed.

The experiment was also conducted on the tms-tbf starting material but this material was not in a crystalline form as for Tbf, this is seen on the left in figure 7.23. The material was again heated as in the fabrication

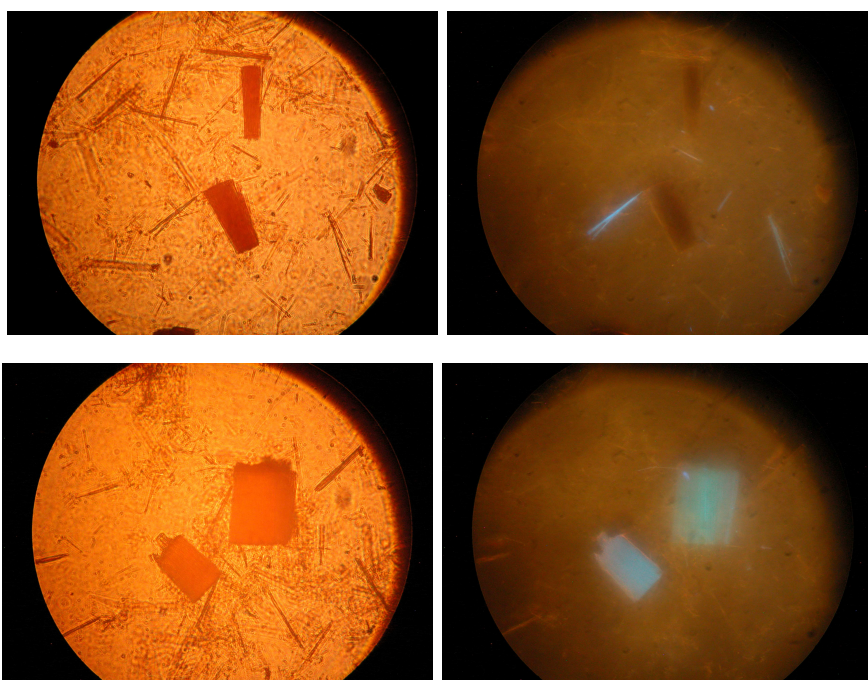


Figure 7.21: Illustration of the optical difference between tbf nanostructures. The left side images are made with white transmission light. The right side are a combination of white transmission light and UV excitation centered at 365 nm. It is easy to see that not all of the nanostructures are fluorescent.

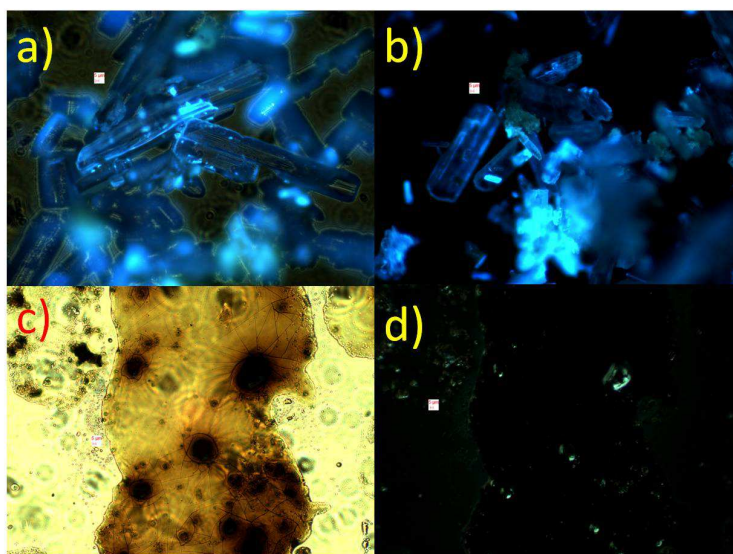


Figure 7.22: Images of thermal decomposition of TbF crystals. a) Fluorescence image before heating. b) Fluorescence image after heating with temperature and time as in the fabrication process. The TbF crystals are still intact which indicate that the temperature has to be higher enough to melt the material. c) Additional heating with a temperature 30 degrees above the fabrication temperature. The crystals are now molten but are also brownish in color which could stem from oxidation of the material or impurities. d) Fluorescence image of c) indicating that nearly all fluorescence capability of the material is lost.

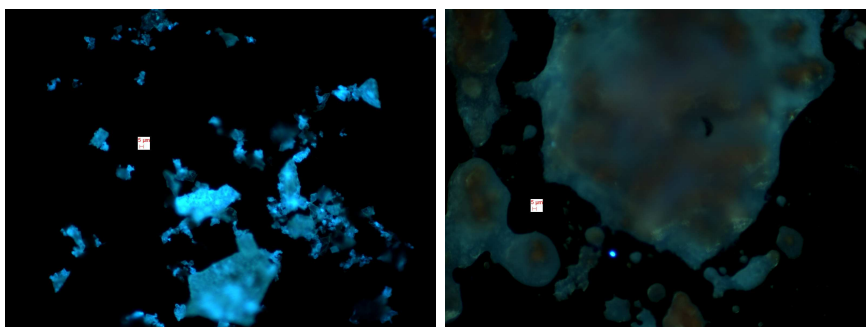


Figure 7.23: Epi-fluorescence images of the tms-tbf starting material drop casted on a glass slide with ethanol. Both images are at 20x magnification and with the excitation centered @365 nm. Left: tms-tbf starting material before heating and with an exposure time of 300 ms. Right: tms-tbf crystal after heating but the exposure time is now 1500 ms.

process of Tms-tbf and the material was molten, as seen on the right in figure 7.23. Spectra of the of the sample were done before and after the heating and is seen in figure 7.24. As seen in both the fluorescence images and in the spectra the heating courses a large loss of fluorescence intensity and from the spectrum it is also seen that it becomes featureless compared to before the heating process. These findings for both Tbf and Tms-tbf indicates that thermal decomposition of the material could play a large role in the observed lack of fluorescence in the fabricated template assisted grown nanostructures.

7.7 Summary

All the investigated samples show clear vibronic structures at low temperature but only p-6P powder and p-6P nanofibers shows vibronic structure at elevated temperatures. The materials for template assisted growth and the nanostructures fabricated by this method show clear broadening of the peaks with increasing temperature. The Huang-Rhys factor for all the structures were calculated and even if thier temperature dependence is different the values found are very similar, as seen in figure 7.25.

It was shown that thermal decomposition could have large influence on the optical quality of the fabricated nanostructures with the template assisted metehod.

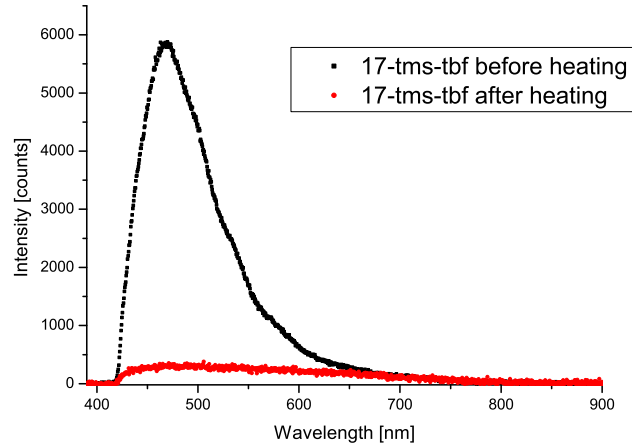


Figure 7.24: Spectra of the tms-tbf starting material before and after heat treatment on the hotplate. Even with a prolonging of the integration time ($t_{\text{before heating}}=100$ ms and $t_{\text{after heating}}=500$ ms) the loss of fluorescence is pronounced and the spectra becomes featureless after heating.

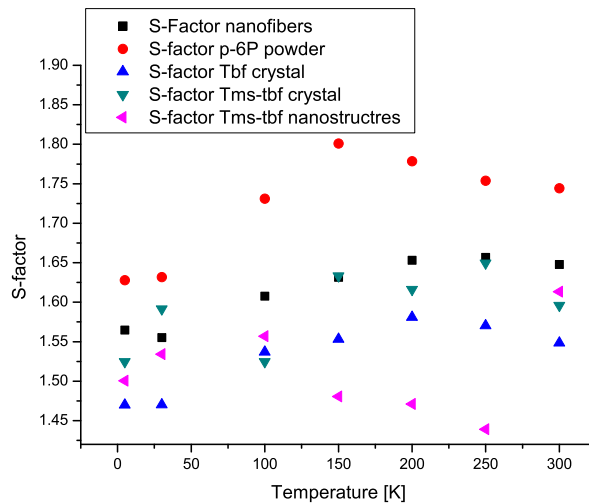


Figure 7.25: The Huang-Rhys factor for all the investigated samples.

Chapter 8

Waveguiding in 1D nanostructures

This chapter describes the waveguiding properties of the two investigated nanostructures. It starts with a short introduction to explain some basic aspects of waveguides and waveguiding based on the following text books[63, 64, 65, 66].

The ability to guide and manipulate the propagation direction of light was first reported experimentally in 1841 by the Swiss physicist Daniel Colladon where he showed that light could be guided in a flow of water by total internal reflection[64]. Since this experiment the field of waveguiding has evolved tremendously and especially fiber optics is now a fundamental and integrated part of modern day society[63, 64]. Optical fibers used today usually have cross sections in the order of several hundred microns and because of their size they are of no use in nano-scaled devices. Optical guides on the nano scale are therefore one of the fundamental problems which has to be solved if the realization of all optical nano devices has to be achieved in the future[67, 68, 69, 70, 46, 71].

8.1 Introduction

Light will, in vacuum or in a linear medium without any external disturbance, propagate in straight lines. This property forms the basis of simple geometrical optics and facilitates simple calculations of optical elements such as lenses, mirrors, microscopes, telescopes etc. Lenses and mirrors can refract and reflect light and thereby change the propagation direction but the light itself will still travel in a straight line to the next optical element. If light has to be bend around corners or guided to a specific place outside of the direct line of sight these optical elements are of little use and this is where the need for optical waveguiding elements comes in.

A waveguide is a structure which directs and confines the wave to propa-

gate along a selected direction and under ideal conditions not lose energy as it propagates. The waveguide is usually designed to a specific type of wave and furthermore also to a specific frequency interval of that particular type of wave. The key elements of a waveguide are a core and the surrounding material called the cladding. The core has a higher index of refraction than the cladding so light that strikes the boundary between the two materials at an angle less than the critical angle is confined in the core by total internal reflection. The difference in indices of refraction does not need to be large to rely on total internal reflection: in optical fibers the difference is usually only about 1%. If the difference in index of refraction is large, more of the light will be guided on the outside of the waveguiding structure than on the inside. These surface waveguides work if they are isolated in air but the waveguide effect is disrupted if there are local changes in the refraction index, for instance objects touching the waveguide or variations in the surface of the structure itself. These local changes will cause some of the guide light to leak out of the waveguide or scatter on imperfections both of which cause an attenuation of the guided light. Another effect which causes attenuation of the guided signal is absorption by the core or cladding material.

The nanostructures investigated in this thesis have no cladding and are laying on a dielectric substrate, so the local environment and imperfections in the nanostructures will have a great influence on the waveguiding properties. The nanostructures are characterized as active waveguides, because the guided light is generated inside the structure and does not have to be coupled to it as in a passive waveguide [46]. Since the nanostructures are active waveguides, the main attenuation effect is due to absorption by the molecules in the waveguide and will dominate the total attenuation of the electric field, which is calculated by:

$$|E(z)| = E_0 e^{-\alpha z} \quad (8.1)$$

where z is the distance the light is guided in the waveguide, E_0 is the field at a reference point and α is the attenuation constant. In the experiments it is the attenuation of the guided intensity which is measured. This quantity is given by:

$$|I(z)| = I_0 e^{-2\alpha z} \quad (8.2)$$

Attenuation is in general a function of the permittivity(ϵ), conductivity (σ), and frequency (ν). Since we investigate dielectric waveguides the conductivity is zero and the attenuation constant is then determined by the frequency and the imaginary dielectric tensor components for the waveguiding material[6]. To calculate the tensor components of the permittivity, Maxwell's equations together with the boundary conditions have to be solved for the specific waveguide. For nanofibers made from p-6P molecules, the theory for calculating the tensor components has been developed[6] and the real part of the dielectric function is known. For the Tbf nanotubes the

theory has not yet been developed and the dielectric function as well as the crystalline structure are not known.

Waveguiding properties of the two different nanostructures will therefore be compared on the basis of experimentally determined attenuation constants of the two systems. Attenuation constants are associated to a specific guided mode of the waveguide and from the theory for the p-6P nanofibers we know that the attenuation constant found in the experiments for the system is connected to the lowest-order TM mode[6]. Since the theory is not developed for Tbf nanotubes the guiding mode spectrum is not known. Hence the attenuation constant found from the experiments are effective ones and might be associated to more than one guided mode.

8.2 Experimental setup for waveguiding

For single photon excited waveguiding in the nanostructures the Nikon ME600D Epi-fluorescence microscope was used. A schematic drawing of the microscope is seen to the left in figure 8.1. For normal use the excitation source illuminates the complete viewing field and the CCD camera records an image of the full viewing field. In this setup the excitation spot is larger than the length dimension of the nanostructures and can't be used to study waveguiding in these nanostructures. By inserting an aperture in front of the mercury (Hg) excitation lamp the excitation spot becomes smaller than the length dimension of the nanostructures and local excitation can be performed, as seen on the right in figure 8.1.

The excitation spot is moved along the nanostructure with high precision by moving the aperture in front of the lamp with fine adjustment screws. Fluorescence images are then recorded at different positions. The CCD camera still records the whole viewing field of the microscope but the excitation spot and the waveguided light scattered at the end of the nanostructure are well separated in the fluorescence images as seen on the left in figure 8.2 and schematically seen on the right in figure 8.1. The fluorescence images are analyzed with the program ImageJ where a line profile is made of the nanostructure, as seen on the right in figure 8.2. The line scan is a readout of the pixel intensity of every point, which in turn is a measure of the fluorescence intensity recorded by the CCD camera. Waveguided intensities from different excitation positions along the nanostructures are collected from the line scans and combined to form an attenuation curve (intensity as a function of distance).

Excitation profile

To remove the influence of the excitation light on the scattered light intensity at the end of the nanostructures the distance between the center of the excitation profile and the end of the structure should be larger than the

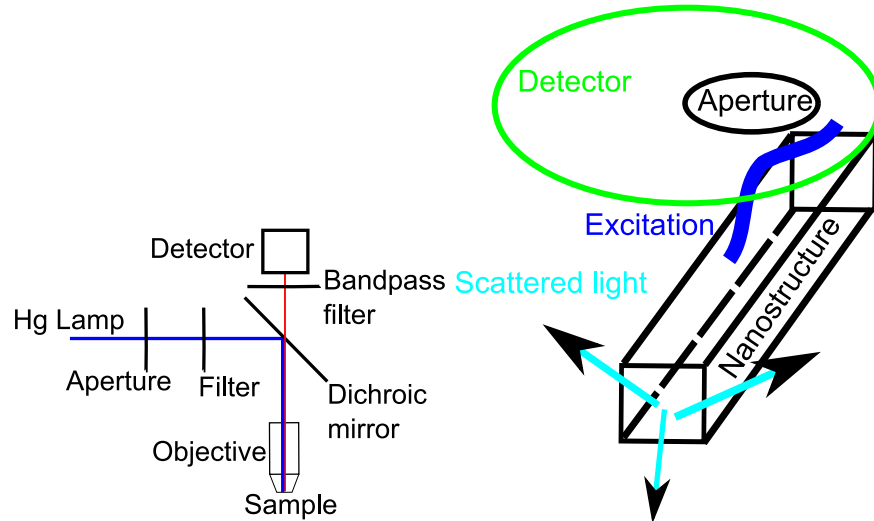


Figure 8.1: Left: Schematic drawing of the Epi-fluorescence microscope with the mounted optical components inside. When the aperture in front of the Hg lamp is closed local excitation of the sample is possible. Right: Schematic drawing of the experimental waveguiding setup. The circles in the top of the drawing marks the diameter of the aperture and the detector.

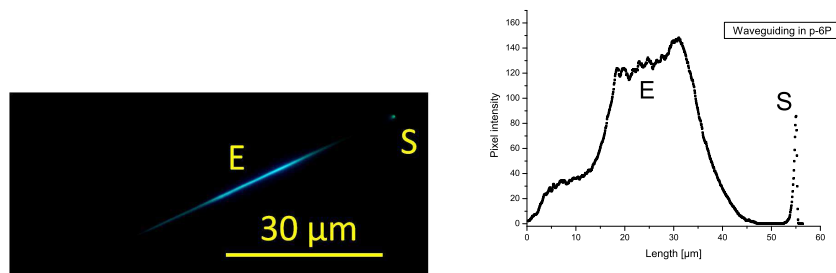


Figure 8.2: Left: Fluorescence image of waveguiding in a p-6P nanofiber on mica. The waveguided light is scattered(S) at the end of the nanofiber 30 μm from the center of the excitation spot(E). The excitation is centered at 365 nm and is provided by a high pressure mercury lamp. Right: A line profile of the nanostructure from the computer program ImageJ. Obviously the excitation profile(E) is well separated from the scattered light at the end(S).

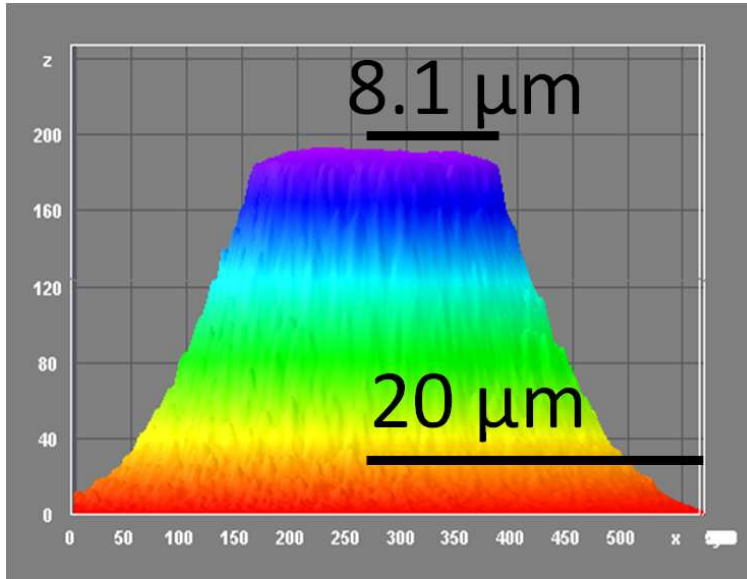


Figure 8.3: Plot of the spatial excitation profile. A 200 nm thick isotropic p-6P film is illuminated by 365 nm light from a Hg lamp with the aperture in front of the lamp closed.

radius of the excitation profile. To estimate the spatial excitation profile an isotropic 200 nm thick para-hexaphenylene film on mica was illuminated and fluorescence images and line scans were done like described above. The resulting plot is seen in figure 8.3. The excitation profile is clearly non-Gaussian and will therefore not be fitted by such a function. The profile has a center plateau of $8.1 \mu\text{m}$ radius with nearly constant intensity and the tail of the profile 'ends' (less than 1 percent intensity) at $20 \mu\text{m}$ from the center. This indicates that the minimum distance between the end of the nanostructure and the center of the excitation profile in the experiments should be $20 \mu\text{m}$.

8.3 Waveguiding in p-6P nanofibers

The p-6P nanofibers are active waveguides and because of reabsorption of the (0-0) transition the wavelength of the propagating light is 425 nm. From theory it is shown that to have at least one propagating mode at 425 nm the p-6P nanofibers should have a width of at least 222 nm[6]. The attenuation constant measured in the experiment is therefore connected to damping of this propagation mode.

Waveguiding in p-6p nanofibers was measured on a sample with nominal thickness of 5 nm. The waveguided intensities are found from a sequence of fluorescence images where three of the fluorescence images are shown in

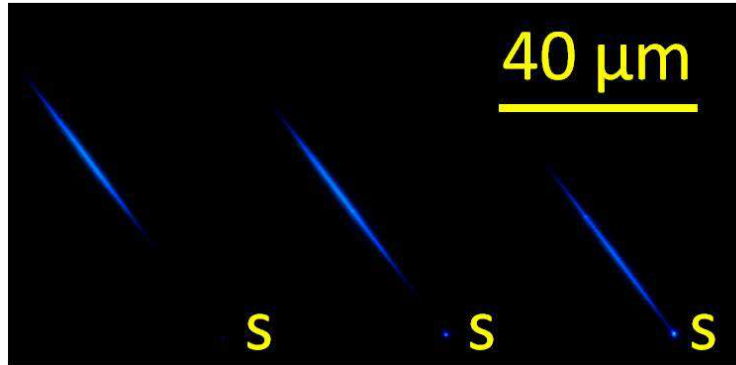


Figure 8.4: Three fluorescence images of the same p-6P nanofiber following local excitation with decreasing distances (left-to-right) between excitation and the scattering(S) at the end of the nanostructure.

figure 8.4. The intensity values are normalized to the intensity measured at the excitation spot and then plotted and fitted in the computer program Origin, as seen in figure 8.5. From the single exponential fit of the data points we get a value of $\alpha_{p-6P} = 0.042$, which is in good agreement to the values that can be deduced from the data plotted in [6, 72]. Other experiments on p-6P nanofibers both from the same sample and from others show similar values for the attenuation constant. From figure 8.5 it can be seen that the p-6P nanofibers are able to guide light over $55 \mu\text{m}$. This value is limited by the experimental setup using the 100x objective. Waveguiding distances up to $100 \mu\text{m}$ have been demonstrated using a 50x objective [6]. The values of the attenuation constants depend of course not on the magnification of the imaging objective.

8.4 Waveguiding in PPTPP nanofibers

In this paragraph waveguiding is demonstrated from nanofibers made from a newly synthesized organic material, PPTPP (2,5-di-biphenylthiophene), deposited on both mica and KCL. For that purpose the laser scanning microscope has been used. Nanofibers made from PPTPP are interesting since they show nonlinear optical properties such as second harmonic generation (SHG), which in the future might be combined with waveguiding properties. Strong SHG was found, see figure 8.6 although the symmetric structure of bulk crystals usually prohibits nonlinear optical processes, thus pointing to a symmetry break in the nanofibers.

Qualitative waveguiding measurements for PPTPP nanofibers are demonstrated in figure 8.7. If one uses UV excitation plus stationary excitation with femtosecond light in the LSM (left-hand side) the green light emitting

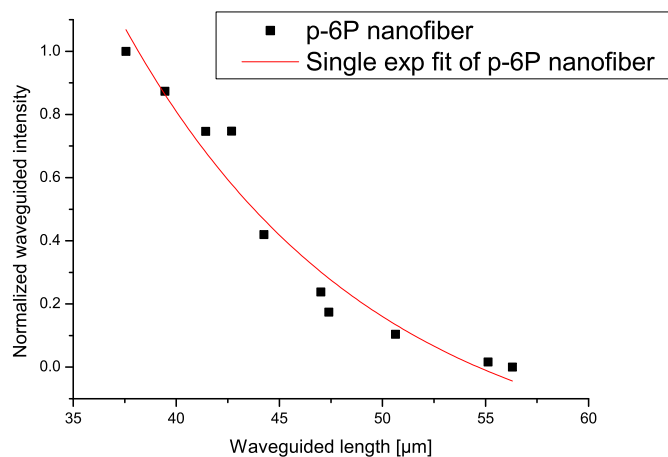


Figure 8.5: Scattered luminescence intensity as a function of the distance from the excitation point for an individual p-6P nanofibers on mica. The single exponential fit of the data points give an attenuation constant of the propagating mode of $\alpha_{p-6P} = 0.042$.

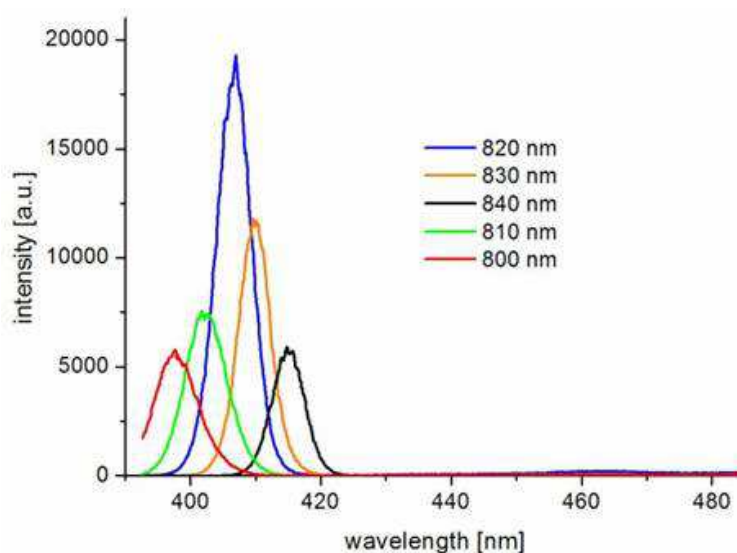


Figure 8.6: Typical second harmonic (SH) signals for different excitation wavelengths for PPTP on mica. The SH peak is up to 100 times greater than the two-photon induced fluorescence, shown around 460 nm. (Collaboration with T.Kawalec, now at Jagiellonian University.)

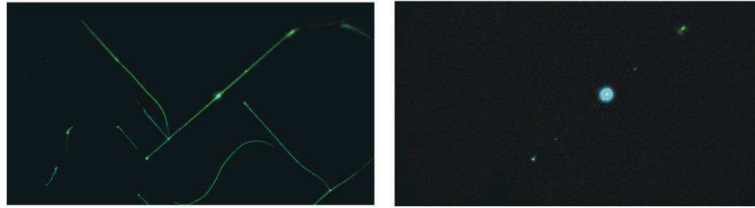


Figure 8.7: Two-photon excited waveguiding properties in PPTPP nanofibers on KCL. The whole sample is additionally illuminated by UV light (left-hand side). Without UV illumination (right-hand-side) only the two-photon excitation spot in the middle of the crystal and the radiated waveguided light at breaks in the nanofibers are present. (Collaboration with T.Kawalec, now at Jagiellonian University.)

fibers can be observed and in addition the two-photon emission in the image center. At breaks in the fibers and at the end of the fibers the light intensity is enhanced. Without the UV excitation only two-photon excited luminescence in the middle of a fiber plus the radiated intensity at breaks is visible (right-hand side). Obviously the two-photon excited green light is generated in the middle of the fiber and is propagating without far field scattering to both ends of the fiber. At breaks and at the end it is scattered and becomes thus visible again in the far field.

The advantage of the LSM for these kind of experiments is that the excitation spot is spatially well defined and that it can be placed easily at different positions along nanoscaled objects.

So far, waveguiding measurements have been performed in the far field using the epifluorescence and the laser scanning microscope. Loss mechanisms in nanofiber waveguides might, however, become more directly visible in the near field. In addition, a scanning near field optical microscope (SNOM) allows one to measure the optical near-field of nanocrystals using evanescent wave excitation. Such a (DMI C-26) SNOM has been implemented and the setup has been designed to find the optimum conditions for light coupling to nanocrystals. The coupling of light is extremely important for the development of photonic micro-devices.

The figure 8.8 shows the first images of nanofibers, transferred to KCL, and seen in the SNOM. The image on the left-hand side is the direct feedback from the SNOM tip, providing morphological information on the fibers. On the right-hand side the corresponding optical image (non-resonant excitation using a HeNe laser) is shown. The non-resonant optical image provides information about the dielectric function of the nanofibers. In future work resonant excitation might be used in the SNOM, thus allowing for investigation of waveguiding in the near field regime. In addition, the combination of characterization techniques should shed light on the origin of the efficient

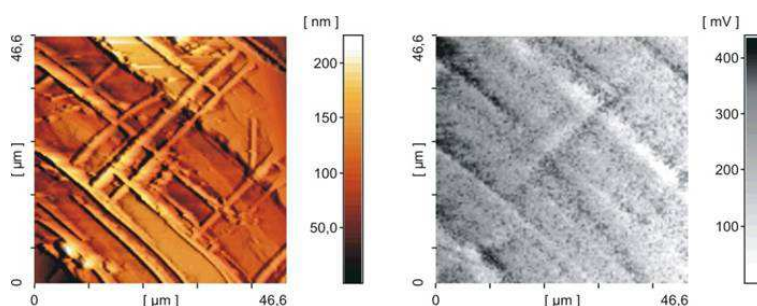


Figure 8.8: PPTPP nanofibers on KCL substrate. Images taken with in the morphology mode (left-hand side) and in the optical mode (right-hand side) of the SNOM microscope upon 633 nm non-evanescent excitation. (Collaboration with T.Kawalec, now at Jagiellonian University.)

SHG process in PPTPP nanocrystals.

Although the results for PPTPP nanofibers are only qualitative, they show that with the instruments developed and optimized in this project it is well possible to obtain complementary new information from the very same type of surface bound nanoaggregates.

8.5 Waveguiding in nanotubes

With single photon excitation waveguiding has only been observed for nanostructures when they are bundled together, whereas this effect has not been seen in a single nanotube. The missing observation of waveguiding in single nanotubes could stem from two reasons; firstly, the amount of material in a nanotube could be so small that the generated and scattered light at the end of a single nanotube is below the detection limit or within the noise of the CCD camera. Secondly, the 100 or 200 nm cross section of the nanotubes, which is determined by the pore size of the template could be too small to sustain propagating modes. Similar to p-6P nanofibers it is expected that the radial cross section of the waveguide has to be above a certain minimum value of the order of half the wavelength of the propagating light. As a result, single photon waveguiding experiments have only been done on bundles of nanotubes.

8.5.1 Waveguiding in Tbf nanotubes

In the experiments Tbf nanotubes were drop casted from solution on a microscope glass slide and two different bundles of waveguiding Tbf nanotubes were found. The waveguided intensities were found for both bundles from sequences of fluorescence images, where three of the images of each bundle are shown in figure 8.9 and figure 8.10. It was observed in the line scans

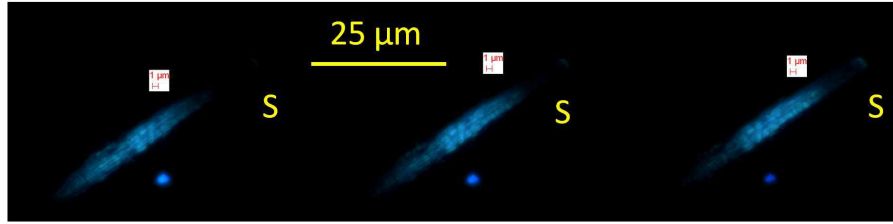


Figure 8.9: Three fluorescence images of bundle 1 of Tbf nanotubes following local excitation with decreasing distances (left-to-right) between excitation and the scattering(S) at the end of the nanostructures. The bundle has a width of $5.8 \mu\text{m}$ and a length of $60 \mu\text{m}$.

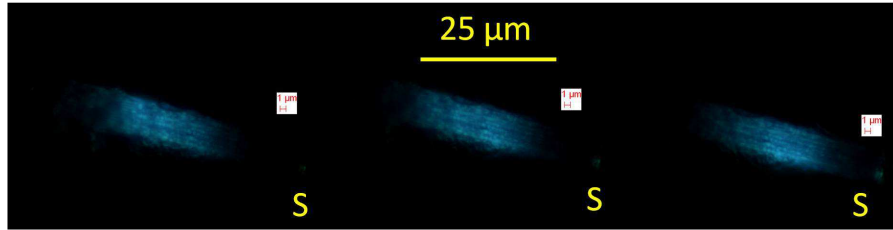


Figure 8.10: Three fluorescence images of bundle 2 of Tbf nanotubes following local excitation with decreasing distances (left-to-right) between excitation and the scattering(S) at the end of the nanostructures. The bundle has a width of $8.3 \mu\text{m}$ and a length of $60 \mu\text{m}$.

that the intensity at the excitation spot was not constant along the bundle of nanotubes. The waveguided intensities could therefore not be normalized to a constant value of the excitation spot as in the case for the p-6P nanofibers but was instead normalized to the largest value of the scattered intensities. This will not change the value of the attenuation constant but change the absolute value of the waveguided intensity. Since the intensity at the excitation spot is not constant along the nanostructure the intensity of the generated light inside the nanotube could also vary influencing the waveguided intensity. The intensity values are plotted and fitted for both bundles of nanotubes, as seen in figure 8.11. From the single exponential fit of both data sets we get the following values for the attenuation constants $\alpha_{Tbf.bundle1} = 0.028$ and $\alpha_{Tbf.bundle2} = 0.068$, values which are very similar to the ones found for p-6P nanofibers.

Since the nanotubes are not isolated like the nanofibers but collected in bundles, the line scan performed in the analysis will cover several nanotubes giving an average value for the attenuation. The above values for the attenuation constants are found for tubes in the middle of the bundles. Line scans were performed in three different positions along Tbf bundle 2. In figure 8.12 scattered luminescence intensity as a function of the distance from the exci-

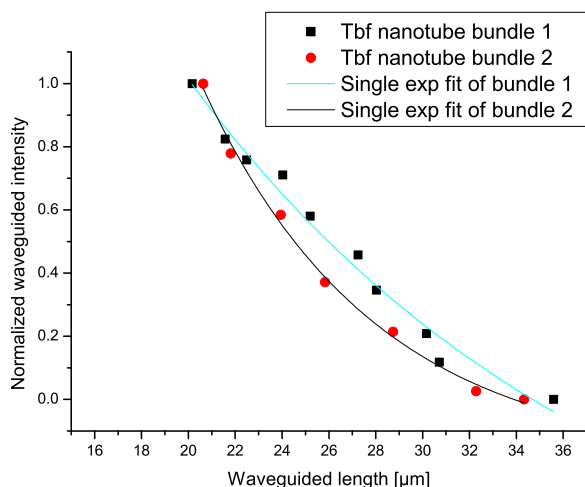


Figure 8.11: Scattered luminescence intensity as a function of the distance from the excitation point for bundles of Tbf nanotubes drop casted from solution. The single exponential fit of the data points gives attenuation constants of the propagating mode of $\alpha_{Tbf.bundle1} = 0.028$ and $\alpha_{Tbf.bundle2} = 0.068$.

tation point for bundle 2 of Tbf nanotubes is seen. From single exponential fit of the data points of each curve three different values of for the attenuation constant are found indicating that the local environment has a great influence on the waveguiding properties of the individual nanotube. Even that the three values of the attenuation constant, $\alpha_{Middle\ of\ bundle} = 0.026$, $\alpha_{Loweredge\ of\ bundle} = 0.036$ and $\alpha_{Higher\ edge\ of\ bundle} = 0.064$ are different they are still comparable to the one found for p-6P nanofibers.

8.6 Waveguiding in Tms-tbf nanotubes

Waveguiding in Tms-tbf nanotubes were investigated in the same manner as described above and three fluorescence images from the experimental sequence are shown in figure ???. In the images it is seen that the light is scattered at both end of the bundle. The line scan was done so the scattered intensity at both ends were recorded and the attenuation constant were found. The two values, $\alpha_{Tms-tbf\ end1} = 0.045$ and $\alpha_{Tms-tbf\ end2} = 0.018$ differs indicating that the local environment has a large influence on the waveguiding behavior of the nanostructures.

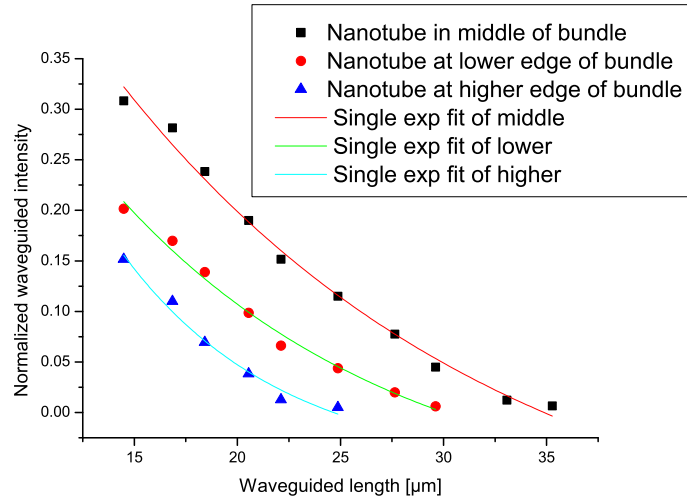


Figure 8.12: Scattered luminescence intensity as a function of the distance from the excitation point for bundles of Tbf nanotubes at three different positions along the bundle. Single exponential fit of the data points of each curve gives attenuation constants of the propagating mode of $\alpha_{Middle\ of\ bundle} = 0.026$, $\alpha_{Lower\ edge\ of\ bundle} = 0.036$ and $\alpha_{Higher\ edge\ of\ bundle} = 0.064$.

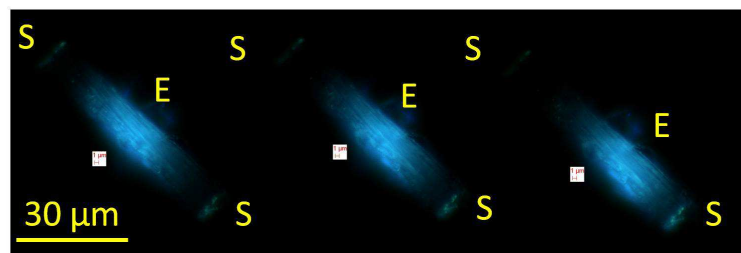


Figure 8.13: Three fluorescence images of a bundle of Tms-tbf nanotubes following local excitation with decreasing distances (left-to-right) between excitation and the scattering(S) at the lower end of the nanostructures. The bundle has a width of $5.5\ \mu\text{m}$ and a length of $60\ \mu\text{m}$. Scattering is observed at both ends of the bundle.

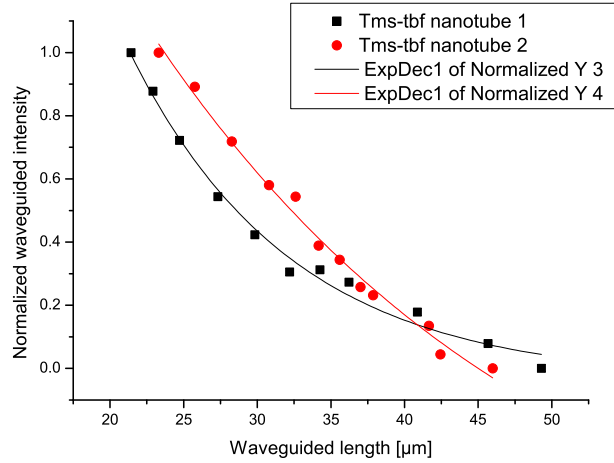


Figure 8.14: Waveguiding in tms-tbf nanotubes measured at two different ends of the bundle. The attenuation constants are $\alpha_{Tms-tbf\ end1} = 0.045$ and $\alpha_{Tms-tbf\ end2} = 0.018$.

8.7 Summary

Optically 1D structures are interesting for several reasons, first the spatial confinement of light, where dimensions are comparable or smaller than the wavelength of the light.

This confinement of the guided light puts restrictions and demands on the type of materials used and especially also on the quality of the structures, i.e the smoothness, regularity, crystallinity, constant size, lack of both structural and material defects and impurities. All these things can contribute to either attenuation, scattering or complete loss of the transmitted light and thereby the signal. In this chapter it was shown that both types of nanostructures are able to guide light with similar attenuation constants. It was further shown that the local environment has a large influence on the waveguiding properties of the nanostructures.

Chapter 9

Conclusions and outlook

9.1 LSM

A LSM has been designed and built at the University of southern Denmark in Sønderborg. The microscope has proven to be a vital characterization tool for optical investigations of nanostructures. With the LSM both single and multi photon process can be studied.

9.2 Low temperature spectroscopy

All the investigated samples show clear vibronic structures at low temperature but only p-6P powder and p-6P nanofibers shows vibronic structure at elevated temperatures. The materials for template assisted growth and the nanostructures fabricated by this method show clear broadening of the peaks with increasing temperature. The Huang-Rhys factor for all the structures were calculated and even if their temperature dependence is different the values found are very similar. It was further shown that thermal decomposition could have large influence on the optical quality of the fabricated nanostructures with the template assisted method.

9.3 Waveguiding

Both types of nanostructures investigated in this thesis were shown to be able to guide light with similar attenuation constants. It was further shown that the local environment has a large influence on the waveguiding properties of the nanostructures.

9.4 Outlook

The template assisted nanostructures should be further investigated and a connection between the morphology and the optical properties should be established. The LSM together with the SNOM should be well suited for these investigations.

Appendix A

Publication list

A.1 Publication list

A.1.1 Refereed

- A. Burchianti, A. Bogi, C. Marinelli, C. Maibohm, E. Mariotti, S. Sanguinetti and L. Moi. Optical characterization and manipulation of alkali metal nanoparticles in porous silica. The European physical journal D 49 (2008) (Highlight paper) also highlight in euophysic-snews 39/6-2008 page 13.

A.1.2 Refereed conference proceeding

- A. Sileikaite, T. Tamulevicius, S. Tamulevicius, M. Andrulevicius, J. Puiso, A. Guobiene, I. Prosycevas, M. Madsen, C. Maibohm and H-G. Rubahn. Periodic structures modified with silver nanoparticles for novel plasmonic application. Nanophotonics II. SPIE. Proc. SPIE, Vol. 6988, 69881Q (2008)

A.1.3 Articles to be submitted

- M.Rastedt, O.N.Frey, C.Maibohm, H.-G.Rubahn, R.Beckhaus and K.Al-Shamery. 17-H-Tetrabenzo[a,c,g,i]fluoren nanotubes, Angewandte Chemie, Int. Ed. (2010)
- C. Maibohm, M.Rastedt, F. Kutscher, O.N.Frey, R.Beckhaus, K.Al-Shamery and H.-G. Rubahn. Low temperature spectroscopy of 8-H-TBF and TMS-TBF, Journal of Luminescence (2010)
- C. Maibohm, M.Rastedt, F. Kutscher, O.N.Frey, R.Beckhaus, K.Al-Shamery and H.-G. Rubahn. Waveguiding in TMS-TBF nanostructures and complexes, App.Phys. A (2010)

- C. Maibohm, M.Rastedt, F. Kutscher, O.N.Frey, R.Beckhaus, K.Al-Shamery and H.-G. Rubahn. Low temperature spectroscopy of TBF /TMS-TBF core-shell nanostructures, J.Luminescence (2011)

A.2 Posters

- 08/08- 2007: Summer school Sønderborg, Denmark. Title: Nanoaggregates, SNOM and LSM
- 22/11-2007: DOPS meeting, Risø, Denamrk. Title: Nanoscaled frequency doubling with organic nanofibers
- 27-31/8-2008: 3rd summer school "European Doctorate in Physics and Chemistry of advanced materials in Palanga, Lithuania. Title: Optical near-field studies of waveguiding organic nanofibers by angular dependent excitation.
- 13-15/07-2009 3rd German-Danish meeting on interface related phenomena, Pappenburg, Germany. Title(s):
17-Trimethylsilyltetrabenzo[a,c,g,i]fluorene-Nanotubes, 17-H-Tetrabenzo[a,c,g,i]fluorene-Nanotubes and Template controlled assembly of Multiwall Molecular Organic Nanotubes (The results were presented on three posters).

A.3 Presentations

- 02/04-2008: Meso-seminar in Sønderborg, Denmark. Title: Raman spectroscopy and SERS.
- 17/04-2008: Talk for ITPD-group, Sønderborg, Denmark. Title: Nanofibers
- 15/07-2008: 2nd German-Danish meeting on interface related phenomena, Sønderborg Denamrk. Title: Laser scanning microscope
- 11/05-2009 Talk for working group in Oldenburg. Title: LSM and waveguiding
- 22/09-2009 Talk for working group in Oldenburg. Title: SEM imaging of Tbf nanostructures
- 20/10-2009 Seminar talk Oldenburg. Title: Waveguiding in Tbf nanostructures
- 17/11-2009 Seminar talk Oldenburg. Title: Waveguiding in Tma-tbf nanostructures
- 11/05-2010 Talk for institute Sønderborg. Title: LSM and template assisted grown nanostructures

- 03/06-2010 Seminar talk Sønderborg. Title: Waveguiding in nanostructures and low temperature spectroscopy

Bibliography

- [1] Matt Law Rong Fan Donald J. Sirbuly, Andrea Tao and Peidong Yang. Multifunctional nanowire evanescentwave optical sensors. *Adv. Mater.*, 19:61, 2007.
- [2] Jong-in Hahm and Charles M. Lieber. Direct ultrasensitive electrical detection of dna and dna sequence variations using nanowire nanosensors. *Nano Letters*, 4(1):51–54, 2004.
- [3] Justin C. Johnson Josh Goldberger Richard J. Saykally Matt Law, Donald J. Sirbuly and Peidong Yang. Nanoribbon waveguides for subwavelength photonics integration. *Science*, 305:1269, 2004.
- [4] Yu-Ming Lin Jennifer Sippel-Oakley Andrew G. Rinzler Jinyao Tang Shalom J. Wind Paul M. Solomon Zhihong Chen, Joerg Appenzeller and Phaedon Avouris. An integrated logic circuit assembled on a single carbon nanotube. *Science*, 311:1735, 2006.
- [5] Justin C. Johnson Richard Saykally Matt Law, Lori E. Greene and Peidong Yang. Nanowire dye-sensitized solar cells. *Nature Materials*, 4:455, 2005.
- [6] F. Balzer, V. G. Bordo, A. C. Simonsen, and H.-G. Rubahn. Optical waveguiding in individual nanometer-scale organic fibers. *Phys. Rev. B*, 67(11):115408–, March 2003.
- [7] F. Balzer; V. G. Bordo; A. C. Simonsen; H. G. Rubahn. Isolated hexphenyl nanofibers as optical waveguides. *Appl. Phys. Lett.*, 82(10), 2003.
- [8] Hisao Yanagi; Takayuki Morikawa. Self waveguiding blue light emission in p-sexiphenyl crystals epitaxially grown by mask-shadowing vapor deposition. *Appl. Phys. Lett.*, 75(2):187, 1999.
- [9] Hisao Yanagi; Takahiro Ohara; Takayuki Morikawa. Self waveguiding gain-narrowing of blue light emission from epitaxially oriented p-sexiphenyl crystals. *Advanced Materials*, 13(19):1452, 2001.

-
- [10] J. Brewer, M. Schiek, A. Lützen, K. Al-Shamery, and H-G. Rubahn. Nanofiber frequency doublers. *Nano Lett*, 6(12):2656–2659, Dec 2006.
- [11] Francesco Quochi, Fabrizio Cordella, Andrea Mura, Giovanni Bongiovanni, Frank Balzer, and Horst-Günter Rubahn. One-dimensional random lasing in a single organic nanofiber. *J Phys Chem B*, 109(46):21690–21693, Nov 2005.
- [12] G. E. Moore. Cramming more components onto integrated circuits. *Electronics*, 38:114, 1965.
- [13] Jonathan Brewer. *Development and biological and nanophysical applications of ultrashort-pulse higher harmonic optical microscopy*. PhD thesis, University of southern Denmark, 2007.
- [14] James B. Pawley, editor. *Handbook of biological confocal microscopy*. Springer, third edition edition, 2006.
- [15] C. Y. Lee R. Colyer and E. Gratton. Frequency-domain fluorescence lifetime imaging microscopy in the photon-counting regime with field-programmable gate arrays. *50th annual meeting of the biophysical society*, 2006.
- [16] F. Balzer; H.-G. Rubahn. Dipol-assisted self assembly of light-emitting p-np needles on mica. *Appl. Phys. Lett.*, 79:3860, 2001.
- [17] F. balzer; V. G. Bordo; A. C. Simonsen; H. G. Rubahn. Optical waveguiding in individual nanometer-scaled organic fibers. *Physical Review B*, 67:115408, 2003.
- [18] T. Haber, M. Oehzelt, R. Resel, A. Andreev, A. Thierry, H. Sitter, D. M. Smilgies, B. Schaffer, W. Grogger, and R. Resel. Single crystalline nature of para-sexiphenyl crystallites grown on kcl(100). *J Nanosci Nanotechnol*, 6(3):698–703, Mar 2006.
- [19] A. Yu. Andreev; C. Teichert; G. Hlawacek; H. Hoppe; R. Resel; D. M. Smilgies; H. Sitter; N. S. Sariciftci. Morphology and growth kinetics of organic thin film deposited by hot wall epitaxy. *Organic Electronics*, 5:23, 2004.
- [20] F. Balzer; H. G. Rubahn. Growth of optically active p-phenylene needles on mica. *Surface Science*, 588:507, 2002.
- [21] J Brewer, C Maibohm, L Jozefowski, L Bagatolli, and H-G Rubahn. A 3d view on free-floating, space-fixed and surface-bound para -phenylene nanofibres. *Nanotechnology*, 16(10):2396, 2005.
- [22] Frank Balzer; Horst-Günter Rubahn. Growth control and optics of organic nanoaggregates. *Advanced Functional Materials*, 15(1):17, 2005.

- [23] F. Meghdadi; S. Tasch; B. Winkler; W. Fischer; F. Stelzer; G. Leising. Blue electroluminescence devices based on parahexphenyl. *Synthetic Metals*, 85:1441, 1997.
- [24] Alejandro L. Briseno, Stefan C.B. Mannsfeld, Samson A. Jenekhe, Zhenan Bao, and Younan Xia. Introducing organic nanowire transistors. *Materials Today*, 11(4):38 – 47, 2008.
- [25] E. Zojer; J. Cornil; G. Leising; J. L. Brédas. Theoretical investigation of the geometric and optical properties of neutral and charged oligophenylenes. *Physical Review B*, 59(12):7957, 1999.
- [26] S. Guha; W. Graupner; R. Resel; M. Chandrasekhar; H. R. Chandrasekhar; R. Glaser; G. Leising. Planarity of para hexaphenyl. *Physical Review Letters*, 82(18):3625, 1999.
- [27] C. Ambrosch-Draxl; J. A. Majewski; P. Vogl; G. Leising. First-principles studies of the structural and optical properties of crystalline poly(para-phenylene). *Physical review B*, 51(15):9668, 1995.
- [28] Peter Puschnig; Claudia Ambrosch-Draxl. Density-functional study for the oligomers poly(para-phenylene): Band structures and dielectric tensors. *Physical Review B*, 60(11):7891, 1999.
- [29] Roland Resel. Crystallographic studies on hexaphenyl thin films-a review. *Thin Solid films*, 433(1-11):1, 2003.
- [30] Kenneth N. Baker; Albert V. Fratini; Timothy Resch; Howard C. Knachel; W. W. Adams; E. P. Socci; B. L. Farmer. Crystal structures phase transitions and energy calculations of poly(p-phenylene) oligomers. *POLYMER*, 34(8):1571, 1993.
- [31] V. E. Klymenko; M. Rozenbaum. Orientations of linear nonpolar molecules in a regular chain. *Journal of Chemical Physics*, 110(12):5978, 1999.
- [32] Andrew C. Hillier; Michael D. Ward. Epitaxial interactions between molecular overlayers and ordered substrates. *Physical Review B*, 54(19):14037, 1996.
- [33] G. Polanski; H. G. Rubahn. Excimer laser assisted growth of au thin films on mica (001). *Journal of vacuum science Technology A*, 14(1):110, 1996.
- [34] F. Balzer; H. G. Rubahn. Chain length dependent para-phenylene film- and needle growth on dielectrics. *Surface Science*, 548:170, 2004.
- [35] K. Müller; C. C. Chang. Electric dipoles on clean mica surfaces. *Surface Science*, 14:39, 1969.

- [36] A. Niko; S. Tasch; F. Meghdadi; C. Brandstätter; G. Leising. Red-green-blue emission of parahexaphenyl devices with color-converting media. *Journal of Applied Physics*, 82(9):4177, 1997.
- [37] Morten Madsen. *Directed growth of organic nanofibers*. PhD thesis, University of Southern Denmark, MCI, NanoSYD, 2009.
- [38] J. Beerman; S. I. Bozhevolnyi; V. G. Bordo; H. .G. Rubahn. Two-photon maps of molecular orientations in hexaphenyl nanofibers. *Optical Communications*, 237:423, 2004.
- [39] Manuela Schiek, Frank Balzer, Katharina Al-Shamery, Jonathan R Brewer, Arne Lützen, and Horst-Günter Rubahn. Organic molecular nanotechnology. *Small*, 4(2):176–181, Feb 2008.
- [40] Zhiyong Fan, Haleh Razavi, Jae-won Do, Aimee Moriwaki, Onur Ergen, Yu-Lun Chueh, Paul W. Leu, Johnny C. Ho, Toshitake Takahashi, Lothar A. Reichertz, Steven Neale, Kyoungsik Yu, Ming Wu, Joel W. Ager, and Ali Javey. Three-dimensional nanopillar-array photovoltaics on low-cost and flexible substrates. *Nat Mater*, 8(8):648–653, August 2009.
- [41] Yongqi Liang, Changgua Zhen, Dechun Zou, and Dongsheng Xu. Preparation of free-standing nanowire arrays on conductive substrates. *J Am Chem Soc*, 126(50):16338–16339, Dec 2004.
- [42] Martin Steinhart, Ralf B Wehrspohn, Ulrich Gösele, and Joachim H Wendorff. Nanotubes by template wetting: a modular assembly system. *Angew Chem Int Ed Engl*, 43(11):1334–1344, Mar 2004.
- [43] M. Steinhart, J. H. Wendorff, A. Greiner, R. B. Wehrspohn, K. Nielsch, J. Schilling, J. Choi, and U. Gösele. Polymer nanotubes by wetting of ordered porous templates. *Science*, 296(5575):1997, Jun 2002.
- [44] Rabih O. Al-Kaysi and Christopher J. Bardeen. General method for the synthesis of crystalline organic nanorods using porous alumina templates. *Chem. Commun.*, pages 1224 – 1226, 2006.
- [45] Charles R. Martin. Membrane-based synthesis of nanomaterials. *Chemistry of Materials*, 8(8):1739–1746, 1996.
- [46] Deirdre O’Carroll, Ingo Lieberwirth, and Gareth Redmond. Melt-processed polyfluorene nanowires as active waveguides. *Small*, 3(7):1178–1183, Jul 2007.
- [47] Zheng Miao, Dongsheng Xu, Jianhua Ouyang, Guolin Guo, Xincheng Zhao, and Youqi Tang. Electrochemically induced sol-gel preparation of single-crystalline tio2 nanowires. *Nano Letters*, 2(7):717–720, July 2002.

- [48] Kai Schröder, Detlev Haase, Wolfgang Saak, Arne Lützen, Rüdiger Beckhaus, Silke Wichmann, and Jürgen Schellenberg. Tetrabenzo[a,c,g,i]fluorenyllithium and \hat{I} -5-tetrabenzo[a,c,g,i]fluorenyltitanium complexes. *Organometallics*, 25(16):3824–3836, 2006.
- [49] Kai Schröder, Detlev Haase, Wolfgang Saak, Rüdiger Beckhaus, Winfried P. Kretschmer, and Arne Lützen. Tetrabenzo[a,c,g,i]fluorenyltitanium(iii) and -(iv) complexes: Syntheses, reactions, and catalytic application. *Organometallics*, 27(8):1859–1868, April 2008.
- [50] Bharat Bhushan, editor. *Handbook of nanotechnology*. Springer, 3rd edition, 2010.
- [51] Silko Grimm, Kathrin Schwirn, Petra Göring, Heiko Knoll, Paul T Miclea, Andreas Greiner, Joachim H Wendorff, Ralf B Wehrspohn, Ulrich Gösele, and Martin Steinhart. Nondestructive mechanical release of ordered polymer microfiber arrays from porous templates. *Small*, 3(6):993–1000, Jun 2007.
- [52] Martin Steinhart, Joachim H Wendorff, and Ralf B Wehrspohn. Nanotubes à la carte: wetting of porous templates. *Chemphyschem*, 4(11):1171–1176, Nov 2003.
- [53] Xiao-Ping Shen, Gui Yin, Cuiling Gao, and Zheng Xu. Construction and fluorescence of organic nanotube arrays by template-based physical vapor deposition method. *Materials Chemistry and Physics*, 113(1):202–207, January 2009.
- [54] Maren Rastedt. Templat gesteuerte erzeugung organischer nanofasern/-röhrchen. Master’s thesis, Oldenburg university, 2008.
- [55] Frauke Kutscher. Neuartige molekulare mehrwandige nanoröhren. Bachelor thesis, Oldenburg university, 2009.
- [56] Mark Fox. *Optical properties of solids*. Oxford, 2001.
- [57] J. D. Wright. *Molecular crystals*. Cambridge, second edition edition, 1995.
- [58] Bernard Valeur. *Molecular fluorescence*. Wiley-VCH, 2002.
- [59] A. Pogantsch F. Balzer and H.-G. Rubahn. Temperature dependent analysis of three classes of fluorescence spectra from p-6p nanofiber films. *Journal of Luminescence*, 8:784–789, 2009.

- [60] A. Kadashchuk H. Sitter C. Winder H. Hoppe S. Sariciftci A. Mura G. Bongiovanni A. Andreev, F. Quochi. Blue emitting self-assembled nano-fibers of para-sexiphenyl grown by hot wall epitaxy. *phys. stat. sol. (a)*, 10:2288–2293, 2004.
- [61] Y. T. Yau C. M. Martin M. Chandrasekhar H. R. Chandrasekhar R. Guentner P. Scanducci de Freitas S. Guha, J. D. Rice and U. Scherf. Temperature-dependent photoluminescence of organic semiconductors with varying backbone conformation. *Phys. Rev. B.*, 67, 2003.
- [62] Rabih O. Al-Kaysi, Tarek H. Ghaddar, and Gonzalo Guirado. Fabrication of one-dimensional organic nanostructures using anodic aluminum oxide templates. *Journal of Nanomaterials*, page 14, 2009.
- [63] F. Graham Smith and Terry A. King. *Optics and photonics, An introduction*. Wiley, 2000.
- [64] Jeff Hecht. *Understanding fiber optics*. Prentice Hall, 2002.
- [65] Grant R. Fowles. *Introduction to modern optics*. Dover publications, 1975.
- [66] John David Jackson. *Classical electrodynamics*. Wiley, third edition edition, 1999.
- [67] Melissa Fardy and Peidong Yang. Materials science: lilliputian light sticks. *Nature*, 451(7177):408–409, Jan 2008.
- [68] Xiujuan Zhang, Xiaohong Zhang, Wensheng Shi, Xiangmin Meng, Chunsing Lee, and Shuitong Lee. Single-crystal organic microtubes with a rectangular cross section. *Angew Chem Int Ed Engl*, 46(9):1525–1528, 2007.
- [69] Yong Sheng Zhao, Jinjie Xu, Aidong Peng, Hongbing Fu, Ying Ma, Lei Jiang, and Jiannian Yao. Optical waveguide based on crystalline organic microtubes and microrods. *Angew Chem Int Ed Engl*, 47(38):7301–7305, 2008.
- [70] Deirdre O’Carroll and Gareth Redmond. Pollyfluorene nanowire active waveguides as sub-wavelength polarized light sources. *Physica E*, pages 2468–2473, 2008.
- [71] Yong Sheng Zhao, Hongbing Fu, Aidong Peng, Ying Ma, Qing Liao, and Jiannian Yao. Construction and optoelectronic properties of organic one-dimensional nanostructures. *Acc Chem Res*, Dec 2009.
- [72] Rolf Neuendorf Katharina Al Shamery Adam Simonsend Frank Balzer, Vladimir G. Bordo and Horst-Günter Rubahn. Organic nanofibers:

a new window to optics of ultrasmall aggregates. *PROCEEDINGS OF THE SOCIETY OF PHOTO-OPTICAL INSTRUMENTATION ENGINEERS (SPIE)*, 5118:263–270, 2003.